Materials Horizons

ROYAL SOCIETY OF CHEMISTRY

REVIEW

View Article Online
View Journal | View Issue

Cite this: *Mater. Horiz.*, 2025, **12**, 7221

Recent progress in perovskite photodetectors: from carrier dynamics to device structures and applications

Ya Mo,[ab] Xiaoyue Huang,[c] Qian Hu,[c] Chuanqun Hu,[c] Paul K. Chu[d] and Jia Li*[b]

Received 7th January 2025,
Accepted 15th May 2025

DOI: 10.1039/d5mh00032g

rsc.li/materials-horizons

Electronic devices have undergone tremendous development recently due to the advent of perovskites. The excellent semiconducting properties of perovskites make them important candidates for innovative and disruptive applications such as photodetectors. The combination of large absorption coefficients, tunable bandgaps, and superior carrier mobilities renders perovskite materials highly desirable for high-performance photodetectors in image sensing, optical communication, environmental monitoring, and medical detection. To date, a variety of perovskites ranging from quantum dots, two-dimensional materials, and polycrystalline films to single crystals have been incorporated into two- or three-terminal devices to demonstrate the superior photodetection performance in terms of responsivity, detectivity, noise, linear dynamic range, and response speed. In particular, great success has been made in the broadband photodetection region spanning gamma-ray, X-ray to ultraviolet-visible-near infrared (UV-Vis-NIR) light. In this review, we provide a comprehensive overview of the recent progress of perovskite-based photodetectors. Beginning with discussing the carrier dynamics and elucidating the mechanisms of photo-induced carrier generation, transport, and recombination, the versatile device architectures, beneficial material properties, tailored perovskite microstructures, and carrier dynamics are subsequently described. The objective of this review is to not only shed light on the basic design principle of perovskite photodetectors in terms of the carrier dynamics, but also serve as a roadmap for further development of perovskite photodetectors in medicine, industry, and life science.

Wider impact

Perovskite materials with high absorption coefficients, tunable band gaps, high carrier mobilities, high photoelectric conversion efficiencies and other optoelectronic properties show great application potential. Therefore, studying the physical properties of perovskite materials and their carrier mechanisms is very important for the construction of their optoelectronic devices. The study of perovskite carrier dynamics in order to determine their physical characteristics is of great significance for optimizing device performance and constructing new structures. In addition, by summarizing different types of perovskite photodetectors in recent years, we can promote the research of perovskite photodetectors and their applications in different fields. This paper reviews the physical properties of perovskite materials revealed using different carrier dynamics methods, and summarizes the recent research on different perovskite photodetectors and their applications in different fields. Combining these aspects paves the way for the development of future perovskite photodetectors with better performances and greater sensitivities.

1. Introduction

A photodetector converts optical signals into detectable electrical signals *via* the photoelectric effect. The performance of a photodetector varies depending on the photosensitive materials and device structure, which affect factors such as the detection range, response speed, and sensitivity. High-performance photodetectors have extensive applications in fields such as medicine, optical communications, image sensing, and environmental monitoring.[1–4]

Perovskite materials are crystalline substances with the general chemical formula of ABX_3, where A represents a large-radius

[a] *College of Applied Technology, Shenzhen University, Shenzhen 518060, China*
[b] *College of Engineering Physics, Shenzhen Technology University, Shenzhen 518118, China. E-mail: lijia@sztu.edu.cn*
[c] *School of Materials and Chemical Engineering, Hubei University of Technology, Wuhan 430068, China*
[d] *Department of Physics, Department of Materials Science and Engineering, and Department of Biomedical Engineering, City University of Hong Kong, Tat Chee Avenue, Kowloon, Hong Kong, China*

organic or metal cation, B is typically a metal ion, and X is a halogen anion. These components form a network of interconnected cubes or octahedra at their vertices.[5] This structure endows the perovskite materials with outstanding electrical, optical, and magnetic properties.[6–8] Furthermore, they exhibit high carrier mobility, excellent light absorption, and tunable energy band gaps,[9–11] making them highly desirable for photoelectric conversion devices.[12] As the photoelectric conversion efficiency of perovskite-based devices continues to improve, a good understanding of their carrier dynamics is crucial for the further development and optimization of perovskite photodetectors.[13]

In this review, we describe the carrier dynamics and explore the influence of microstructural factors on carrier generation in perovskite materials. We also review the synthesis and applications of novel perovskite photodetectors. This review aims to provide a comprehensive background and guidance for the future development of high-performance perovskite optoelectronic devices.

2. Perovskite carrier dynamics

The dynamic parameters of perovskite carriers, such as the carrier lifetime, mobility, and diffusion length, impact the properties of photodetectors. For instance, the carrier lifetime determines the distance photogenerated carriers can travel before recombination, thus affecting the response speed and sensitivity. A long carrier lifetime improves the gain and responsiveness of a photodetector, but an excessively long lifetime may produce a slower response. The carrier mobility affects the carrier transport efficiency, and high mobility improves the response speed and current output of the photodetector.

2.1. Generation, composite, and transmission mechanisms of charge carriers

Perovskite charge carriers are free charge carriers primarily consisting of electrons and holes. Energy transfer triggered by photoexcitation or an electric field can cause electrons to transition from the valence band to the conduction band[14,15] thus generating free electrons and holes. The mechanism of the generation of these charge carriers is vital to the carrier dynamics in perovskite materials. Liu *et al.*[16] investigated the photoexcited carrier dynamics of iodine-doped $MAPbBr_3$ single crystals using excitation intensity-dependent steady-state photoluminescence (PL) and time-resolved photoluminescence (TRPL) and revealed that carrier diffusion influences the photoexcited carrier dynamics and that shallow electron traps affect the PL dynamics. This study provides a good understanding of the fundamental properties of mixed halide perovskite materials.

In perovskite materials, electrons and holes recombine and release energy. The recombination influences the photoelectric properties of the materials and determines the lifetime of charge carriers. Charge-carrier recombination in perovskites occurs by several mechanisms, including radiative, nonradiative, Auger, and surface recombination.[17–20] Nonradiative recombination is the primary pathway for carrier relaxation and leads to reduced photoluminescence quantum efficiency.[21] Yao *et al.*[22] demonstrated that the addition of aminopropionic acid to perovskite solar cells inhibits nonradiative recombination. Aminopropionic acid not only regulates the crystal growth of $CH_3NH_3PbI_3$ films but also minimizes film defects to enhance both photoluminescence and electroluminescence, giving rise to a longer carrier lifetime and suppressed nonradiative recombination. Consequently, the efficiency of the solar cells increases by approximately 15%. Similarly, Liu *et al.*[23] have used cesium sulfate (Cs_2SO_4) to modify the SnO_2 interface and improve the growth of perovskite crystals. Cs_2SO_4-modified SnO_2 shows enhanced charge extraction and higher conductivity, as indicated by a reduced defect density and suppressed non-radiative recombination. The modification improves the carrier extraction and efficiency in addition to a 1.15% increase in the conversion efficiency as well as greater device stability.

When materials absorb photons, the photon energy causes electrons in the valence band to transition to the conduction band and form electron–hole pairs. Electrons are excited to the conduction band and become free electrons that can migrate freely in the materials, whereas holes in the valence band lead to positively charged carriers. This process excites electrons from the valence band to the conduction band, so perovskite materials can conduct electricity and participate in photoelectric conversion. However, in some cases, the transitioned electrons and holes remain in the form of 'excitons' that attract each other through Coulomb forces. Excitons are bound states of electrons and holes that cannot move freely. Only under sufficient energy offset and external electric fields will they efficiently separate into free carriers. The electrons and holes move from their generation sites to the heterojunction interfaces, *e.g.*, bulk heterojunction or planar heterojunction, and are collected by the electrodes to generate the photocurrent. The migration mechanism involves carrier mobility and diffusion. A high carrier mobility enables rapid movement in the materials to improve the device performance, whereas a longer diffusion length allows for a more effective collection of photogenerated carriers to improve the photoelectric conversion efficiency.[24,25] Zang *et al.*[26] developed quasi-two-dimensional tin perovskite films using mixed monoammonium and diammonium terminal ligands. The diammonium ligands reduce the total number of terminal ligands, delay film growth, and improve the film orientation. This approach enhances both the carrier mobility and diffusion length, resulting in a 14.3% increase in conversion efficiency (Fig. 1). Li *et al.*[27] studied iodide 3D $FA_{0.8}Cs_{0.2}PbI_3$ and discovered the 2D/3D perovskite heterostructures passivated by a higher ordered 2D perovskite have lower Urbach energy. Urbach energy is a key parameter for measuring the internal disorder in materials, and the smaller the value, the fewer material defects and the steeper the absorption edge. A low Urbach energy reduces non-radiative recombination and dark currents caused by defects and improves the carrier collection efficiency, device responsiveness, signal-to-noise ratio, and detection sensitivity, ultimately

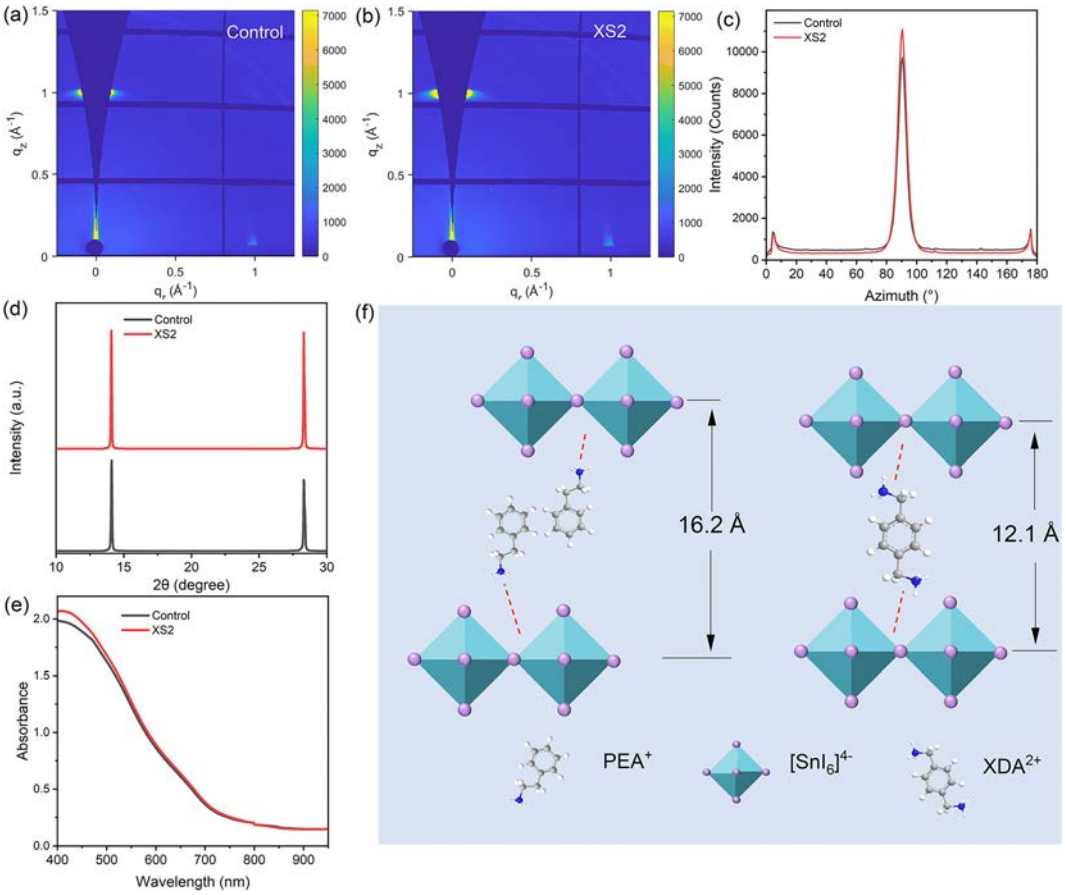

Fig. 1 Characterization of perovskite crystal structures: (a) GIWAXS patterns of the control films and (b) XS2 films with an incident angle of 0.5°; (c) GIWAXS intensity integrated azimuth at q = 1 Å^{-1}. (d) XRD patterns and (e) Abs spectra of the control and XS2 films. (f) Schematic of the interactions between $[SnI_6]^{4-}$ and PEA (left) or XDA (right).[26] (Reproduced from ref. 26 with permission from the Royal Society of Chemistry, copyright 2024.)

increasing the photoluminescence (PL) intensity, PL lifetime, carrier mobility (Φ_μ), and carrier diffusion length (L_D). For instance, the PL lifetime, Φ_μ, and L_D are about 1.3 μs, 18.56 cm^2 V^{-1} s^{-1}, and 7.85 μm, respectively.

More specifically, the photodetection performance metrics can be formulized by the fundamental parameters of carrier dynamics. For instance, the photoresponsivity (R) of a perovskite phototransistor can be determined by the formulas $R = I_{pc}/(P_{inc}S)$, where I_{pc} is the photocurrent, P_{inc} is the incident light intensity, and S is the channel area of the device. The phototransistor can operate in either photoconductive mode or photovoltaic mode, depending on the relationship between gate voltage (V_g) and threshold voltage (V_{th}). When $V_g > V_{th}$, the phototransistor operates in photoconductive mode, and the photocurrent can be expressed as $I_{pc} = (q\mu_p pE)WD$, where q is the elementary charge, μ_p is the carrier mobility, p is the charge concentration, E is the electric field within the channel, W is the channel width, and D is the depth of light absorption. When $V_g < V_{th}$, the phototransistor operates in photovoltaic mode leading to the photocurrent $I_{pc} = g_m\Delta V_{th} = AKT\ln(1 + \eta q\lambda P_{opt}/I_{pd}hc)/q$, where η is the quantum efficiency, g_m is the transconductance, ΔV_{th} is the threshold voltage displacement, I_{pd} is the dark current, P_{opt} is the incident light power, hc/λ is the photon energy, A is the proportional parameter, K is Boltzmann's constant, and T is the temperature. Clearly, the carrier dynamics plays a critical role in determining key performance metrics. The efficiency, speed, and noise characteristics of a photodetector are directly governed by carrier dynamics. It is of vital importance to understand and optimise the dynamics (*e.g.*, minimizing recombination, enhancing transport, and improving extraction) by engineering the material microstructures or by designing the appropriate device architecture to achieve high-performance perovskite photodetectors.

2.2. Effects of microstructures on charge carriers

The microstructures of perovskite materials, including the crystal structure and defect types, influence the carrier generation, migration, and recombination properties.[28,29] Defects and grain boundaries in perovskite materials affect the carrier recombination rate and reduce the photoelectric conversion efficiency. High-quality crystal structures with low defect densities show markedly improved carrier lifetime and mobility.[30,31] These defects can be categorized into two distinct types: those originating from the chalcogenide film (referred to as body defects) and those concentrated at the surface and interface of the chalcogenide film (designated as surface defects).

Body defects include point and grain boundary defects, whereas surface defects include dangling surface bonds and interface defects. To reduce the defect density and improve the crystalline quality of chalcogenide films, chemical passivation, surface modification, introduction of additives, crystallization regulation, and other methods have been proposed for defect regulation. Liao *et al.*[32] applied a lithium fluoride (LiF) surface modification layer to the outermost perovskite layer to reduce trap states and facilitate the formation of interface dipoles. The modification resulted in a 20.31% increase in the short-circuit current density of the IPHC devices. Interface engineering offers new insights into optimizing the performance of IPHCs and conventional perovskite-based solar cells. Yuan *et al.*[33] incorporated an aqueous gold nanorod solution into the perovskite active layer to form a composite by one-step spin coating. The addition of water promotes film crystallization and film quality and suppresses carrier recombination. This approach increases the short-circuit current density (*J*sc) from 21.03 to 21.6 mA cm^{-2}, the fill factor (FF) from 78.65% to 82%, and the power conversion efficiency (PCE) from 18.02% to 19.46%. Wan *et al.*[34] utilized a hot-casting deposition method to create RP polycrystalline perovskite $(BA)_2(MA)_3Pb_4I_{13}$ films with excellent crystal orientations (Fig. 2). They developed a 2D hybrid perovskite photodetector (PD) in which spontaneous polarization and light coupling enhance light-induced carrier dissociation and adjust carrier transport. The thermo-optoelectronic effect results in a current approximately 35 times greater than the photovoltaic effect current at a bias of 0 V. The photodetector exhibits a responsivity of 12.7 mA W^{-1}, a detectivity of 1.73×10^{11} Jones, and an on/off ratio of 3.97×10^3. Li *et al.*[35] proposed a modified spatial restriction method to control nucleation and growth by adjusting the heating area. This method produces $MAPbBr_3$ single crystals (SCFs) with sizes exceeding 30 mm and controllable thicknesses of 15–45 μm. The controlled growth kinetics results in higher crystallinity, larger photoinduced carrier density, and longer carrier lifetime than the corresponding bulk single crystals (BSCs).

The microstructure of perovskite materials is closely related to its stability, and the integrity and number of defects in the crystal structure affect the chemical, thermal, moisture, and light stability. The ABX_3 crystal structure of perovskites determines its carrier migration and photoelectric properties but

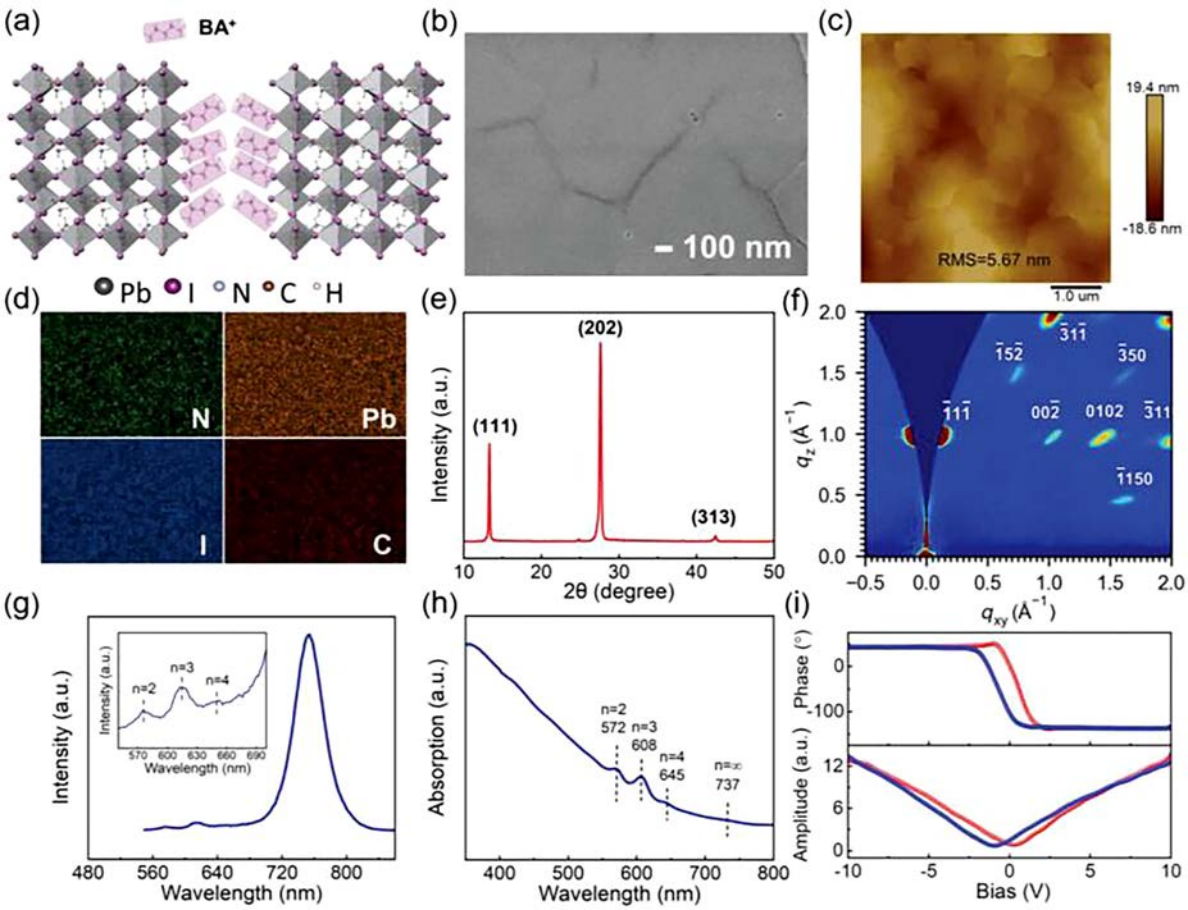

Fig. 2 Characterization of the 2D polycrystalline perovskite $(BA)_2(MA)_3Pb_4I_{13}$ film: (a) crystal structure of the $(BA)_2(MA)_3Pb_4I_{13}$ layered perovskite; (b) and (c) SEM and AFM images; (d)–(f) EDS maps, XRD patterns, and GIWAXS maps of the polycrystalline $(BA)_2(MA)_3Pb_4I_{13}$ perovskite film; (g) and (h) photoluminescence and absorption spectra of the 2D perovskite film; (i) PFM hysteresis loops.[34] (Reproduced from ref. 34 with permission from the John Wiley and Sons, copyright 2023.)

makes it susceptible to environmental factors. The choice of A-site cations and B-site metal ions affects the stability of the lattice. Smaller A-site cations or more active B-site metals can lead to structural relaxation or oxidation. Moreover, X-halogens have important effects on lattice stability, and the type of halogen ion determines the reactivity of a material in different environments. Crystal defects, surface inhomogeneity, and built-in electric fields enhance the erosion of perovskite by water and light and accelerate degradation. Optimizing the microstructure, such as by reducing defects, selecting stable ion combinations, and improving interface design, is the key to improving the stability of perovskites and extending their service life. For example, Mo *et al.*[36] synthesized $CsPbBr_3$@ZrO_2 nanocrystals in room temperature and improved their stability by coating ZrO_2 onto the $CsPbBr_3$ nanocrystals. The photoluminescent quantum yield (PLQY) of the $CsPbBr_3$@ZrO_2 nanocrystals reaches 80%. White LEDs made of the $CsPbBr_3$@ZrO_2 nanocrystals have a light effect of up to 64.0 Lm W^{-1}, making them suitable for visible light communication. Zhao *et al.*[37] designed and prepared a lead-free metal halide ($(C_{12}H_{28}N)_2Cu_2I_4$) with a zero-dimensional (0D) structure and synthesized single crystals (SCs) by heating a precursor solution. The photoluminescence quantum yield (PLQY) is as high as 87.0% in conjunction with a large Stokes shift and long PL decay time. After storing for 36 days in 70% humid air, the PL intensity decreases by only 10%, thus demonstrating good air stability. Due to the double self-trapping exciton (STE) mechanism of the $[Cu_2I_4]^{2-}$ cluster, $(C_{12}H_{28}N)_2Cu_2I_4$ has excellent optical properties and stability as X-ray scintillators. Zhao *et al.*[38] synthesized leadless metal halide Rb_2CuX_3 (X = Cl, Br) at room temperature. The Rb_2CuX_3 powder exhibits high purple emission dominated by the self-trapping exciton (STEs) mechanism. The PLQY values of Rb_2CuCl_3, $Rb_2CuCl_{1.5}Br_{1.5}$, and Rb_2CuBr_3 are 73.12%, 65.25%, and 28.63% respectively. The Rb_2CuX_3 powder delivers excellent performance in terms of heat, UV light, humidity, and mechanical stability. These characteristics make the materials appealing to wireless optical communication and X-ray imaging. Wang *et al.*[39] synthesized $CsCu_2I_3$ monocrystals with a cm size using a saturated precursor cycling crystallization method and placing them in a saturated high-temperature precursor solution to grow large monocrystals through gradient cooling crystals. The $CsCu_2I_3$ single crystals exhibit a high absorption coefficient, a bandgap of 3.17 eV, and an average PL life of 571.96 ns, indicating fewer internal defects. These crystals also have good thermal, light, and chemical stabilities.

2.3. Time-resolved spectroscopy for the study of charge carrier dynamics

Time-resolved spectroscopy has been extensively used to study carrier dynamics, as it offers information about carrier generation, migration, recombination, and decay. Common time-resolving techniques include time-resolved photoluminescence spectroscopy, transient absorption spectroscopy, and time-resolved photoelectron spectroscopy.[40–42] These methods impart valuable temporal information regarding the behavior of charge carriers in materials.

2.3.1. Time-resolved photoluminescence (TRPL). Time-resolved photoluminescence (TRPL) spectroscopy involves the use of femtosecond or picosecond laser pulses to excite materials and the monitoring of the emitted light as carriers recombine. This technique provides information about the carrier properties by monitoring the changes in the photoluminescence intensity with time. Qiu *et al.*[43] have used transient absorption spectroscopy and TRPL to quantify carrier reorganization, diffusion, and extraction in printable mesoscopic perovskite solar cells (p-MPSCs) to show that the carrier diffusion length in perovskite materials can reach 5.48 μm in the mesoscopic scaffold and establish the relationship between maximum quasi-Fermi level splitting and the perovskite materials. Xiao *et al.*[44] used steady-state photoluminescence (PL) spectroscopy, TRPL, and time-resolved microwave optoelectronics (TRMC) to study radiative and non-radiative processes in $MAPb(Br_{1-y}I_y)_3$ solar cells. Their results show that the electron and hole capture rates in mixed-halide perovskites are higher than those in single-halide perovskites, indicating that mixed halide crystals have additional capture densities for both electrons and holes. The work enhances the understanding of the carrier recombination process in mixed halide perovskite solar cells. Pandey *et al.*[45] investigated the carrier dynamics in hybrid perovskites ($(FA_{0.83}MA_{0.17})0.95Cs_{0.05}Pb(I_{0.83}Br_{0.17})_3$) by TRPL and ultrafast transient absorption spectroscopy (TAS). The average carrier lifetime increases from 3 to 19 ns under continuous illumination. Additionally, the carrier recombination time decreases from 226 to 66 ps during illumination for 30 minutes, demonstrating that surface perovskite films can be used for micro-strain regulation and carrier dynamics studies. Zhao *et al.*[46] combined PL, TRPL, and ultrafast transient absorption (TA) measurements to explore the diffusion and transfer imbalances between electrons and holes in $Cs_2AgBiBr_6$ perovskite solar cells (PSCs) and proposed mesoporous TiO_2 (ETL) as an electron transport layer to address these imbalances. This approach improves the conversion efficiency by over 24%, compared to using only a compact TiO_2 ETL as well as the energy storage capacity. Due to the inherent defects and indirect bandgap of $Cs_2AgBiBr_6$ film, the PL strength of PVK film is relatively low, and the TRPL results are consistent with those of PL. The TA spectra of PVK, PVK-SPIRO, and PVK-PCBM at different time delays indicate that all the TA spectra show negative bleaching signals at approximately 440 nm (Fig. 3). Alharbi *et al.*[47] have studied the effects of adding methylammonium triiodide (MAI_3) to perovskite precursor solutions for defect passivation. By means of TRPL and time-resolved terahertz spectroscopy (TRTS), it is shown that MAI_3 reduces nonradiative recombination, increases charge carrier mobility, and enhances device stability.

2.3.2. Transient absorption spectroscopy. In transient absorption spectroscopy, the charge carrier dynamics is monitored by detecting the absorption changes at different time points upon stimulation as charge carriers alter the light absorption properties of materials. Jo *et al.*[48] investigated the photoinduced carrier dynamics of perovskite films under atmospheric conditions using ultrafast time-resolved transient absorption spectroscopy. There are three decay modes, carrier

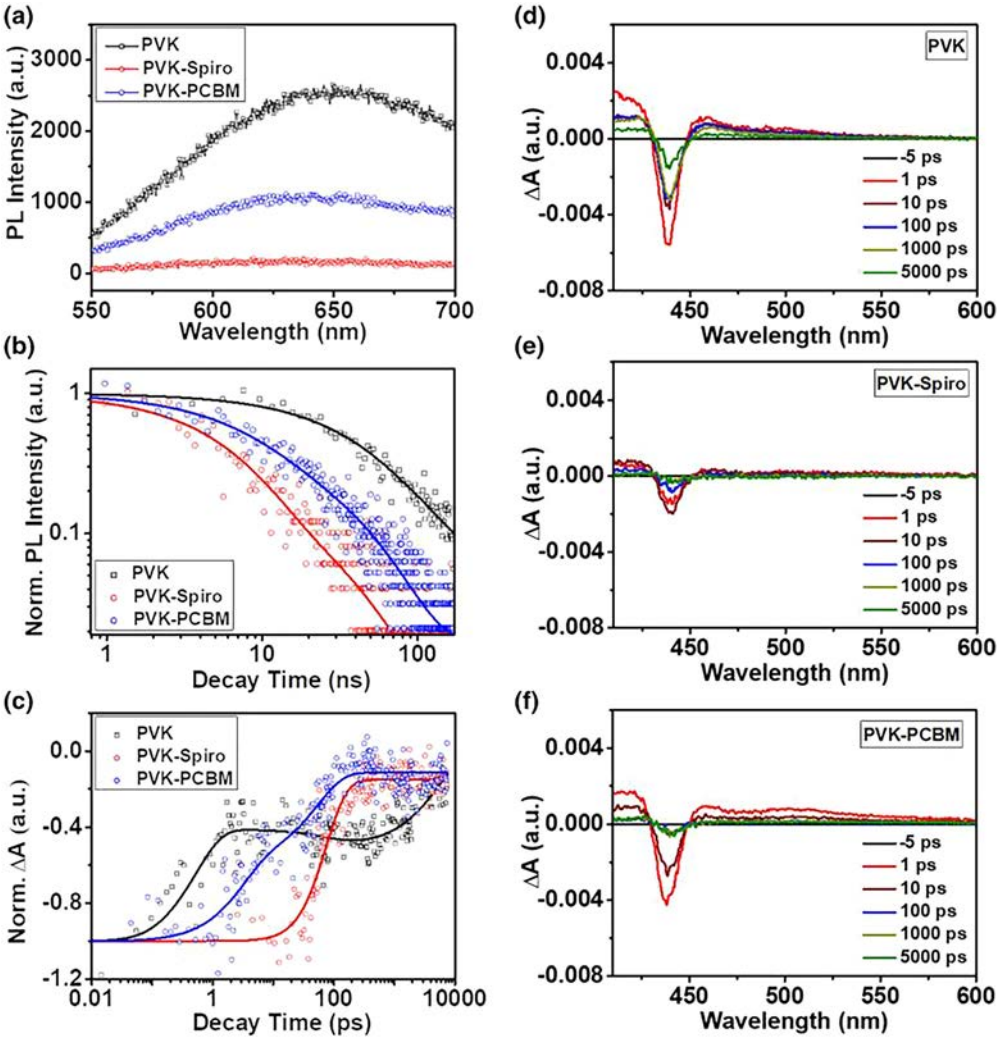

Fig. 3 (a) PL spectra and (b) normalized TRPL spectra of quartz/$Cs_2AgBiBr_6$, quartz/$Cs_2AgBiBr_6$/spiro-OMeTAD, and quartz/$Cs_2AgBiBr_6$/PCBM thin films excited by 400 nm irradiation (100 fs, 1 kHz, approximately 2.1 μJ cm^{-2}); (c) normalized bleaching kinetics of quartz/Cs2AgBiBr$_6$, quartz/$Cs_2AgBiBr_6$/spiro-OMeTAD, and quartz/$Cs_2AgBiBr_6$/PCBM thin films probed at 442 nm. Transient absorption spectra of (d) quartz/$Cs_2AgBiBr_6$, (e) quartz/$Cs_2AgBiBr_6$/spiro-OMeTAD, and (f) quartz/$Cs_2AgBiBr_6$/PCBM thin films upon excitation by 360 nm irradiation (100 fs, 1 kHz, approximately 1.5 μJ cm^{-2}).[46] (Reproduced from ref. 46 with permission from the John Wiley and Sons, copyright 2022.)

capture, carrier extraction, and carrier recombination, and the atmospheric conditions slow and reduce carrier extraction to degrade light-harvesting. Increasing the carrier density in the perovskite film restores the decay rate in the reduced carrier extraction mode. Singh *et al.*[49] carried out femtosecond time-resolved pump–probe transient absorption spectroscopy (TAS) to examine ultrafast carrier extraction in two-dimensional/three-dimensional (2D/3D) bilayer perovskite solar cells (PSCs). The formation of a quasi-equilibrium state leads to sub-band absorption with an ultrafast lifetime of 440 fs. The short-lived feature gives rise to the local electric-field-induced electroabsorption, resulting in an enhanced power conversion efficiency in 2D/3D PSCs. Duan *et al.*[50] used transient absorption spectroscopy (TAS) to explore the photogenerated carrier relaxation process in organic–inorganic perovskite $Cs_xMA_{1-x}PbI_3$ materials with varying x values (Fig. 4). Fig. 4(a) and (b) show the TAS of $MAPbI_3$ and $Cs_{0.1}MA_{0.9}PbI_3$ perovskite at different delay times, respectively. The TAS showed two main characteristic spectra: transient photo-induced absorption signals in the range of 520–700 nm, and a ground-state bleaching signal appearing around 750 nm. Surface Cs^+ doping affects the perovskite crystal structure and regulates the carrier dynamics. The appropriate A-cation doping not only preserves the crystal phase but also extends the lifetime of photogenerated carriers. Dehury *et al.*[51] investigated the optical nonlinearity as well as excited-state carrier dynamics of femtosecond laser-induced organometallic halide ($(C_{12}H_{25}–NH_3)_2PbI_4$) two-dimensional colloidal nanoparticles (NPs) and their films using ultrafast transient absorption spectroscopy. By studying the room-temperature Mott-type exciton dynamics and carrier recombination characteristics, information on ground-state bleaching and light-induced absorption regions is provided. Shen *et al.*[52] examined the transient absorption spectra of $CsPbX_3$ nanomaterials using a femtosecond laser to study the carrier dynamics by

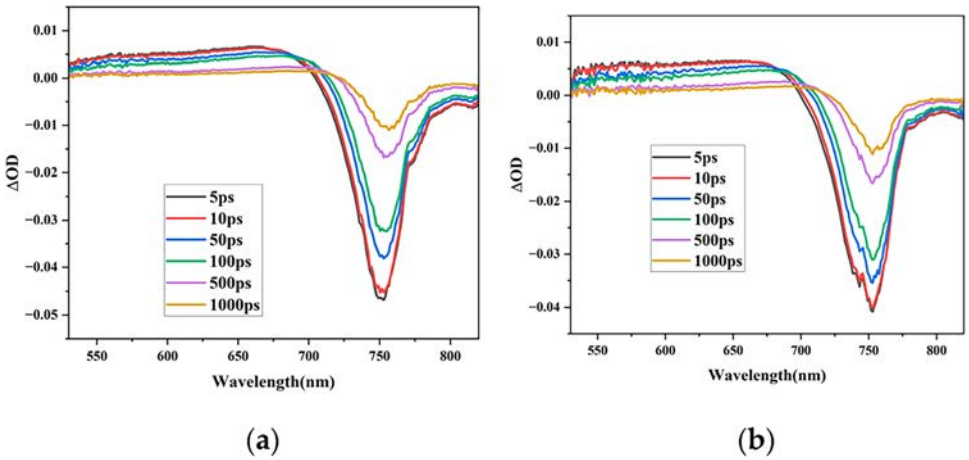

Fig. 4 TAS at different delay times after excitation at 400 nm: (a) $MAPbI_3$ perovskite and (b) $Cs_{0.1}MA_{0.9}PbI_3$ perovskite.[50] (Reproduced from ref. 50 with permission from the MDPI, copyright 2023.)

varying excitation power and delay time. An initial redshift of 5–12 nm in the bleaching signal of the TA spectra is observed followed by stabilization. With increasing excitation power, the bleaching signal exhibits a distinct fast decay component, indicating the presence of double exciton states. In perovskite materials, the strong coulomb interactions between electrons and holes lead to significant exciton–exciton coupling. Upon activation, the first exciton interacts with subsequent excitons to promote two free excitons from a single exciton state to a biexciton state. Because the energy required for the formation of the second exciton is lower than that required by the initial exciton, the overall system energy decreases, resulting in a redshift in the emission spectrum. The binding energy of a biexciton can be determined by comparing the wavelengths of the bleaching signals of the single exciton and biexciton states.

2.3.3. Time-resolved photoelectron spectroscopy. Time-resolved photoelectron spectroscopy involves exciting electrons to a free state *via* the photoelectric effect and measuring the temporal changes in their energy distribution. Rieger *et al.*[53] performed time-resolved photoelectron spectroscopy to investigate the carrier dynamics and diffusion on surfaces and observed that the electron mobilities of ordered $CsPbBr_3$ (001) and $CsSnBr_3$ (001) films at room temperature are 31 ± 6 cm^2 V^{-1} s^{-1} and 13 ± 1 cm^2 V^{-1} s^{-1}, respectively. At 90 K, the mobility of $CsPbBr_3$ (001) increases to 200 ± 8 cm^2 V^{-1} s^{-1}, suggesting strong electron–phonon coupling at the conduction band minimum. Evans *et al.*[54] acquired femtosecond time-resolved two-photon photoemission (TR-2PPE) and transient reflection (TR) spectra to investigate the initial electron cooling and polaron formation kinetics of the single crystal $CsPbBr_3$ perovskite (Fig. 5). The increase in the surface polaron formation rate with temperature is related to the broadening of phonon resonance, indicating that phonon disorder and dephasing promote the formation of large polarons. Liu *et al.*[55] combined femtosecond pump–probe with photoemission electron microscopy (PEEM) to study trap states in $CsPbBr_3$ single crystal microplates with spatiotemporal energy resolution and revealed that shallow traps exhibit high defect tolerance, but deep traps affect the surface dynamics. Ultrafast PEEM provides a comprehensive view of rapid electron transfer and the accumulation of surface trap states. Lin *et al.*[56] applied pump–probe technology to analyze the carrier dynamics in the electron transport layer (ETL) and hole transport layer (HTL) of perovskite solar cells and observed reduced carrier recombination and shorter injection lifetimes in perovskite solar cells modified with an optimized transport layer, giving rise to better power conversion efficiency.

A close relationship exists between chalcogenide photodetectors and solar cells. There are similarities in their device structures, and it has been demonstrated that the photovoltaic conversion efficiency of a solar cell can be significantly improved by optimizing the crystalline quality and defect density of the chalcogenide film. The same applies to photodetectors, and their response speed and sensitivity can be improved. Perovskite materials are often used in devices such as photodetectors due to their exceptional photoelectric properties. Although both perovskite-based solar cells and photodetectors share advantages such as a high light absorption coefficient and an adjustable bandgap, their design philosophies differ significantly. Solar cells function as "energy collectors", prioritizing steady-state high output, whereas photodetectors act as "signal sensors", focusing on transient response and sensitivity. Further investigation into the perovskite carrier dynamics is crucial, as it not only guides materials modification but also enhances the understanding and utilization of perovskite materials in photodetectors.

3. Preparation of perovskite-based photodetectors

A photodetector converts light into electrical signals by the photoelectric effect[57,58] *via* the absorption of photon energy from incident light, generation and migration of light-induced

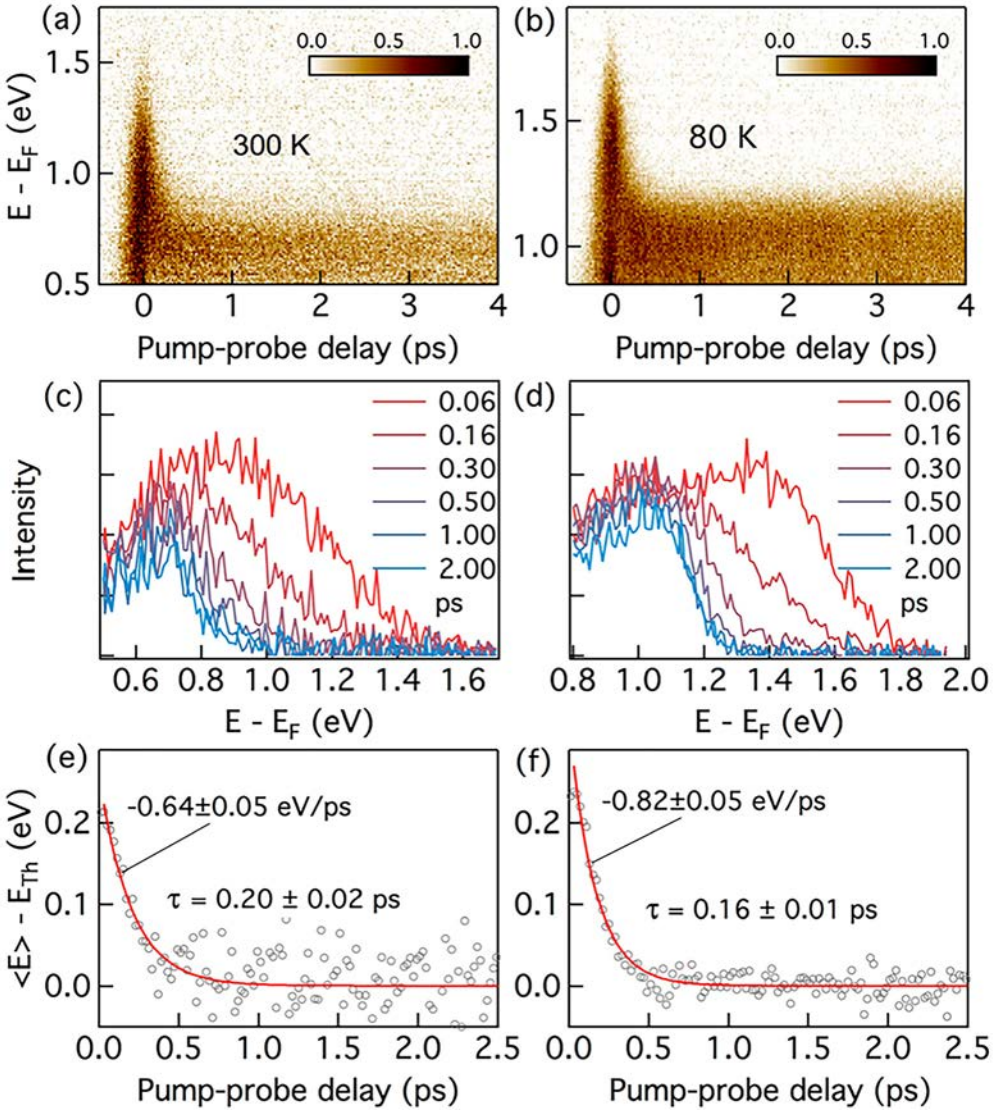

Fig. 5 Hot electron cooling probed by TR-2PPE: (a) and (b) 2D pseudo color (intensity) plot of TR-2PPE spectra as a function of electron energy and pump–probe delay for single-crystal $CsPbBr_3$ at (a) 300 K and (b) 80 K; (c) and (d) electron energy distribution curves (at representative pump–probe delays (Δt = 0.06–2.0 ps) at 300 K and 80 K; (e) and (f) mean energy of the electron distribution as a function of the pump–probe delay at 300 K and 80 K, where the mean electron energy (E) is referenced to the thermalized electron energy, E_{Th}, at long pump–probe delays ($\Delta t \geq 4.0$ ps).[54] (Reproduced from ref. 54 with permission from the American Chemical Society, copyright 2018.)

carriers, and signal processing to form an electrical signal. This conversion process has applications in various fields, including medical imaging, environmental monitoring, and communication security.[59–61] Perovskite materials, with their high optical absorption coefficients and excellent carrier mobility,[62–64] contribute to the superior performance of perovskite photodetectors. Depending on the operating principles, perovskite photodetectors can be classified into four types: photoconductor (Fig. 6(a)), photodiode (Fig. 6(b)), phototransistor (Fig. 6(c)), and photomultiplier.[65–68]

3.1. Photoconductors

A photoconductor is an optoelectronic device based on the photoconductivity effect that is capable of converting incident light into an electrical signal. When photosensitive materials are exposed to light, the electrical conductivity increases significantly, thereby changing the current or voltage in the circuit and achieving the detection of light intensity. When a bias voltage (external electric field) is applied to both ends of a photoconductive photodetector, the photogenerated carriers move directionally under the action of the electric field to form a photocurrent. The magnitude of the photocurrent is proportional to the light intensity. Zhao *et al.*[69] developed a planar photoconductive photodetector using a $CH_3NH_3PbI_3$ ($MAPbI_3$)/IDT-BT/MoO_3 structure. The IDT-BT and MoO_3 layers enhance hole transport and improve the dissociation efficiency of electron–hole pairs. Moreover, MoO_3 acts as an electron barrier to reduce the dark current. This device exhibits a rapid response

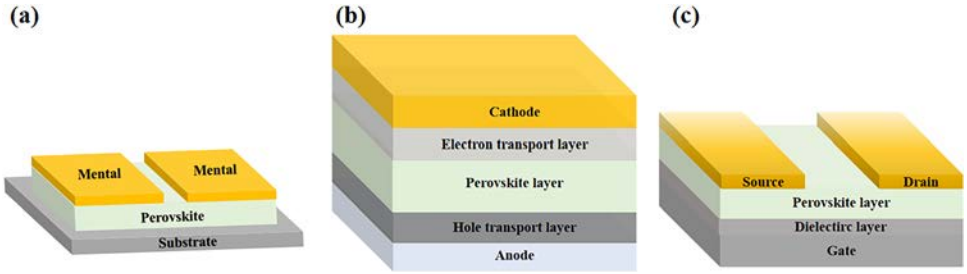

Fig. 6 The architecture schematic of (a) perovskite photoconductor; (b) perovskite photodiode; and (c) perovskite phototransistor.

time of less than 7 ms, a high responsivity of 11.6 A W^{-1}, and an exceptionally high detectivity of 5.2 × 10^{13} Jones. Guan *et al.*[70] incorporated zeolitic imidazolate framework nanoparticles (ZIF-11 and ZIF-23) into an organic–inorganic perovskite $MAPbI_3$ film. The addition of ZIF-11 and ZIF-23 enhances the crystal quality, and the ZIF-23-doped photodetector shows an photoresponsivity of 0.164, a detectivity of 3.27 × 10^{12} Jones, and stable operation at a bias voltage of 1.2 V. Sun *et al.*[71] used a masking method and channel width tuning to create a photoconductive detector (PCD) based on the Ag-$MAPbI_3$-Ag structure showing a high responsivity of 45.5 aW^{-1}, detectivity of 7 × 10^{12} Jones, and fast response time of 0.35 ms. This detector is integrated into an optical communication system for effective byte transmission. Shen *et al.*[72] prepared a negative single-layer graphene photodetector (NPC) using chemical vapor deposition (CVD) and deposited perovskite $FAPbI_3$ quantum dots on graphene to create a positive photoconductive (PPC) photodetector, which shows a responsivity of 8.03 A W^{-1} under UV light and a detectivity of 1.89 × 10^{10} Jones. Chen *et al.*[73] fabricated an all-inorganic $CsPbBr_3$ film by a low-temperature solution method and developed an optical conductivity detector with digital inter-patterned gold electrodes. Due to the efficient photoinduced carrier generation and rapid extraction with minimal leakage currents, the $CsPbBr_3$-based photodetector has fast photoresponses with a decay time of 0.213 s and a rise time of 0.233 s (Fig. 7). Huisman *et al.*[74] synthesized $CsPbBr_3$ using dry mechanochemical methods in the presence of polybutyl methacrylate (PBMA). The powder is heated and pressed into disks and then layered onto a glass substrate in a cross-electrode pattern to create a planar photoconductive device. This device achieves a detectivity of up to 2 × 10^{11} Jones. By adjusting the thickness of the disk, the narrow-band detection capability of the device is optimized as the more focused charge collection allows for fine-tuning of the position and width of the peak. Zhi *et al.*[75] developed a straightforward method to synthesize two-dimensional (2D) fully inorganic $CsPb_2Br_5$ nano/microsheets at room temperature and explored their use as active layers in solution-treated photodetectors. The $CsPb_2Br_5$ nano/microsheets serve as the active layer in a photoconductive photodetector, which shows a high specific detectivity of 1.0 × 10^{12} Jones, a photoresponsivity of 0.02 A W^{-1}, and an ultra-low dark current of 10^{-12} A under 405 nm illumination. Liang *et al.*[76] synthesized phase-pure 2D $(PEA)_2FAPb_2I_7$ (where PEA = $C_8H_{11}N$ and FA = CH_4N_2) by inhibiting the formation of 3D perovskite phases. The 2D Ruddlesden–Popper (RP) layered metal halide perovskite films are used to create a photoconductive photodetector with a high detectivity of over 9.4 × 10^{12} Jones. Cottam *et al.*[77] utilized defect-assisted high optical conductivity gain in graphene transistors to enhance fully inorganic cesium lead halide perovskite nanocrystals (NCs). The photoconductive gain in the UV-visible wavelength range results from charge transfer between the nanotubes and graphene, resulting in a remarkable photoconductive gain of 10^6 A W^{-1}. Liang *et al.*[78] prepared large-area, uniform $SrZrS_3$ films by sputtering with high crystallinity with a distorted orthorhombic structure and the *Pnma* space group. The optical absorption coefficient of $SrZrS_3$ exceeds 10^5 cm^{-1}, and its carrier mobility reaches 106 cm^2 V^{-1} s^{-1}. The photodetector based on this symmetric structure shows a high responsivity of

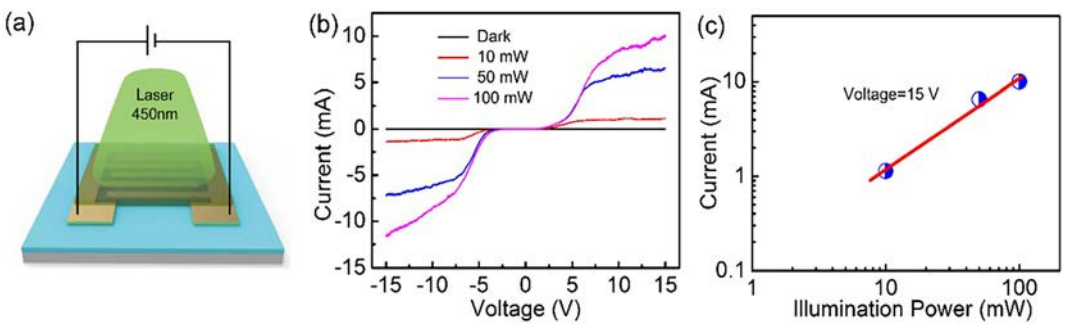

Fig. 7 (a) Schematic of a photodetector device composed of $CsPbBr_3$ thin films; (b) *I*–*V* curves measured in the dark and under illumination using a 450 nm laser diode by sweeping the voltage from −15 to 15 V; (c) logarithmic plot of the photocurrents *versus* illumination power.[73] (Reproduced from ref. 73 with permission from the Elsevier, copyright 2021.)

8 A W^{-1} under 405 nm optical excitation. Shil *et al.*[79] synthesized all-lead-inorganic $Cs_3Sb_2X_9$ (X = I, Br) perovskite films by two-step chemical vapor deposition (CVD) and fabricated photoconductive devices. The $Cs_3Sb_2I_9$ and $Cs_3Sb_2Br_9$ films exhibit responsivity of 54.5 and 3.6 mA W^{-1} and detectivity of 4.3×10^{10} and 1.6×10^{10} Jones, respectively. The $Cs_3Sb_2I_9$ film photodetector has stable photoelectric switching properties with rise and decay times of 50 and 30 ms and 108 ms and 56.2 ms for $Cs_3Sb_2I_9$, respectively. These findings highlight the broad applicability of crystalline $Cs_3Sb_2I_9$ perovskite films in optoelectronic devices.

3.2. Photodiodes

Photodiodes are optoelectronic devices based on the photovoltaic effect. They are distinct from photoconductive detectors because they can directly convert light into electricity (photovoltaic voltage or current) without an external bias voltage. The basic device consists of a PN junction which separates the photogenerated carriers using an electric field and converts the optical energy into an electrical signal. Duan *et al.*[80] improved the crystal quality of the perovskite layer using a SiW_9Co_3@rGO composite prepared from polyformaldehyde and graphene derivatives. The perovskite films have an average grain size of 1222.92 nm. The photodetector shows a photocurrent of 43.94 μA in addition to excellent stability, boding well for photovoltaic applications. Wang *et al.*[81] enhanced the sequential deposition process of perovskite crystals to produce films with a low defect density and high quality. Improved crystallization and surface defect passivation lead to a peak power conversion efficiency (PCE) of over 23% for the perovskite solar cells. The perovskite photodetector exhibits a responsivity of 0.49 A W^{-1} and a linear dynamic range of up to 136.75 dB. Ding *et al.*[82] conducted morphological engineering on the broad gap inorganic 2D perovskite $Cs_2PbI_2Cl_2$ by creating *in situ* self-supported nanosheet structures with optimal charge channels. These structures are incorporated into the photovoltaic-type self-driven photodetectors that exhibit lower dark current and more efficient charge collection. The device shows a responsivity of up to 698 mW cm^{-2} and a detectivity of 8.6×10^{12} Jones (Fig. 8). Yang *et al.*[83] prepared a high-quality $MAPbI_3$ film and incorporated 1D ferroelectric perovskite $TMIMPbI_3$ to create a self-powered, flexible, and stable photodetector based on a 1D/3D hybrid perovskite ferroelectric thin film/P3HT heterojunction. The photodetector delivers improved photoelectric performance with a dark current of 7×10^{-9}A, responsivity of 6.6 mA W^{-1}, and detectivity of 5×10^9 Jones. Additionally, the device has good folding durability and wet stability. Zhang *et al.*[84] prepared a photodetector by integrating $MA_{0.6}FA_{0.4}PbI_{3-x}Cl_x$ halide perovskite polycrystals with β-NYF_4:Yb/Er upconversion nanoparticles. The detector shows a high responsivity of 0.52 A W^{-1} at 985 nm and stability for 2000 cycles. Tao *et al.*[85] produced a self-powered optical detector based on the $FAPbBr_3/NiO_x$ heterostructure for sensitive X-rays and optical detection. The photodetector shows exceptional optical response upon 450 nm light irradiation, such as a high photoresponsivity of 123.6 mA W^{-1}, detectivity of 7.1×10^{11} Jones, and fast response/recovery times of 10/200 ns. This photodetector also displays a photovoltaic effect of 0.80 V and a

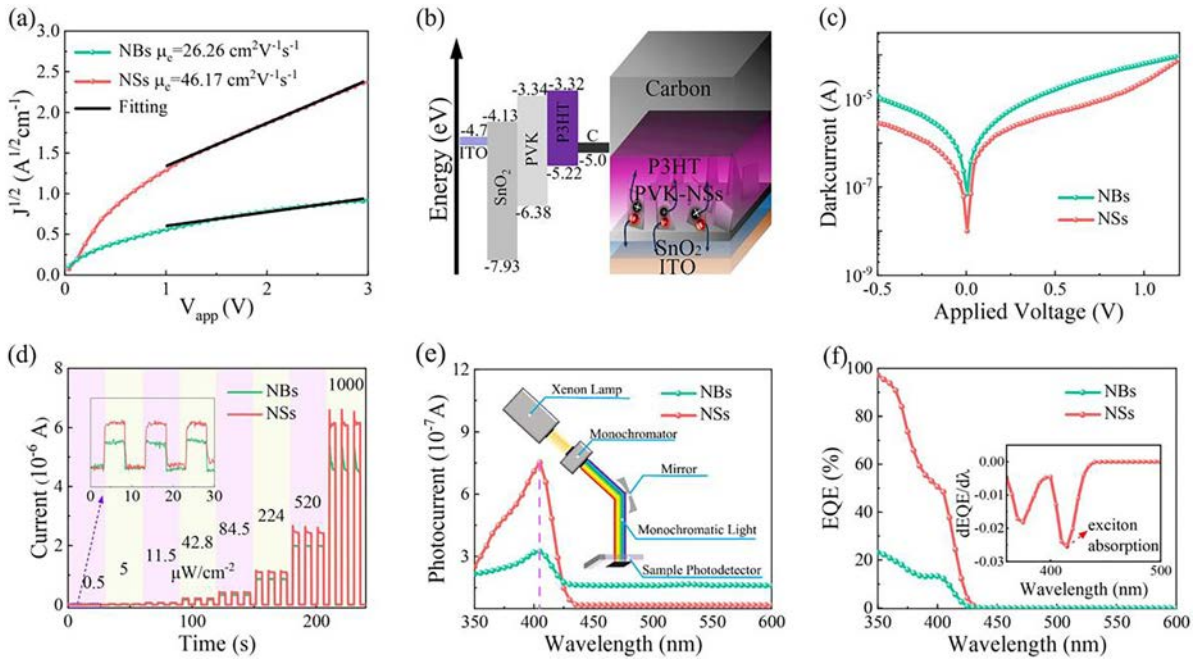

Fig. 8 (a) *I–V* curves of the electron-only devices showing the charge mobilities of different structures; (b) schematic of the self-powered photodetector and corresponding energy level alignment; (c) IV properties of the devices in the dark; (d) light response of the two devices illuminated by a 405 nm laser with different intensities from 0.5 to 1 mW cm^{-2}; (e) photocurrents of the two devices at different wavelengths; (f) external quantum efficiency (EQE) of different devices with the inset showing the differentiation of EQE revealing the wavelength of the exciton absorbance response.[82] (Reproduced from ref. 82 with permission from the Elsevier, copyright 2024.)

large carrier mobility lifetime product of 1.1×10^{-3} cm^2 V^{-1}, resulting in superior X-ray sensitivity of 402 μC Gy_{air}^{-1} cm^{-2} at zero bias. Zhang *et al.*[86] prepared a CdS/$MAPbI_3$/spir-OMeTAD heterojunction photodetector using oxygen-doped CdS as an electron transport layer (ETL). This photodetector exhibits stable self-driven characteristics spanning a spectral range of 360–780 nm, photovoltage responsivity increasing from 596.9 to 6383.6 V W^{-1} under 450 nm laser irradiation, and the response spectrum is also extended outside the bandgap restriction of the $MAPbI_3$ to 1550 nm due to both the pyroelectric and photothermoelectric effects. Cheng *et al.*[87] employed a silicon nanoporous column array (Si-NPA) as both a hole transport layer and a growth template to accomplish high-quality conformal growth of $MAPbI_3$ films. The photovoltaic broadband photodetector exhibited an on/off ratio of 0.82×10^5 under zero bias with 780 nm light, a photoresponsivity of 8.13 mA W^{-1}, a specific detectivity of 0.974×10^{13} Jones, and response speeds of 253.3 and 230.4 μs for on and off states, respectively. Yang *et al.*[88] have developed a photodetector with a quasi-2D Ruddlesden–Popper (RP)-layered perovskite film, specifically $PEA_2FA_2Pb_3Br_{10}$. This photodetector benefits from multiple quantum wells, resulting in a low dark current of 4.08×10^{-11} A, a high specific detectivity of 1.69×10^{10} Jones, a high on/off ratio of 7.33×10^3, and rapid rise and fall times of 32 and 38 ms, respectively. Li *et al.*[89] fabricated lead iodide ($FAPbI_3$) photodiodes with and without pseudohalide ions and assessed their performance at room temperature and at liquid nitrogen temperature. The pseudohalide ions enhance the stability and properties as exemplified by a dark current of 10 pA, response time of 50 ns, and detectivity exceeding 10^{12} Jones.

3.3. Phototransistors

Perovskite phototransistors utilize perovskite materials to convert optical signals into electrical signals. These devices typically feature a three-terminal structure: source, drain, and gate. Adjusting the gate voltage modulates the carrier density in the channel to enable the detection and amplification of optical signals. By combining the amplification capabilities of transistors with the photosensitive properties of photoconductors, these detectors exhibit high photosensitivity and gain. Wu *et al.*[90] developed photodetectors using uniformly dense Sn-based perovskite films prepared by solvent engineering. The field-effect transistors exhibit an unusual bipolar transport behavior, with both the electron and hole mobilities exceeding 0.08 cm^2 V^{-1} s^{-1}. These photodetectors achieved a high responsivity of 2.16×10^3 A W^{-1}, a detectivity of 5.16×10^{13} Jones, and fast response in the microsecond range under environmental conditions. Moon *et al.*[91] improved the properties and stability of hybrid photodetectors by using quaternary ammonium ligands (dodecyl dimethyl ammonium bromide, DDAB) for surface passivation. The carrier lifetime of the DDAB-treated $CsPbBr_3$ perovskite quantum dots (DDAB-capped PQDs) is extended by 6.68 to 14.88 ns compared to untreated $CsPbBr_3$ PQDs. A 2D–0D hybrid photodetector is formed by depositing DDAB-capped PQDs onto a WSe_2 field-effect transistor. The photodetector exhibits a responsivity of 1.4×10^3 A W^{-1} and a detectivity of 3.1×10^{13} Jones upon 405 nm laser illumination at 40.0 μW cm^{-2}. Xin *et al.*[92] developed a photon-synaptic sensor using inorganic perovskite quantum dots (QDs) embedded in an InGaZnO (IGZO) thin-film phototransistor. The photodetection wavelength range can be adjusted by varying the halogen ions (Cl and Br) in the perovskite QDs. The $CsPbBr_3$ QD-embedded transistor shows a responsivity of 450 A W^{-1} at 450 nm and 550 A W^{-1} at 550 nm under low-intensity illumination. The perovskite QD-embedded transistors show not only high responsiveness to visible light but also excellent synaptic behavior (Fig. 9). Hou *et al.*[93] developed a hybrid phototransistor consisting of a $CsPbBr_3$ thin film and indium tin oxide (ITO) nanowires (NWs) integrated into InGaZnO channels. By using metal ITO NWs as electron pumps and high-speed channels, the device extracts photocarriers from the $CsPbBr_3$ and injects electrons into InGaZnO. This phototransistor exhibits a responsivity of 4.9×10^6 A W^{-1}, rapid rise and fall times of 0.45 s and 0.55 s, respectively, as well as a high specific detectivity of 7.6×10^{13} Jones. Haque *et al.*[94] fabricated bipolar phototransistors using the organic–inorganic hybrid perovskite $CH_3NH_3PbI_3$. Under white light illumination, the hole and electron currents increase by four orders of magnitude. The dark current recovers quickly after the light source is turned off, thus demonstrating a higher responsivity and shorter response time than previous measurements. Specifically, the phototransistor shows a responsivity of 0.62 A W^{-1}, a response time of 100 ms, and a detectivity of 6.87×10^{15} Jones, whereas the electron current exhibits a responsivity of 0.20 A W^{-1} with a response time of 200 ms in conjunction with a detectivity of 1.33×10^{15} Jones. Haque *et al.*[95] prepared a visible-light phototransistor with a lead iodide/zinc oxide ($CH_3NH_3PbI_3$/ZnO) heterostructure. By adjusting the methyl chloride and precursor ratio ($MAI : PbI_2$), the optical, morphological, and structural properties of the perovskite materials can be tuned. $MAPbI_3$ with the optimal stoichiometric composition ($MAI : PbI_2 = 1 : 1$) shows a responsivity of 234 A W^{-1} and a detectivity of 3.74×10^{13} Jones. Zhang *et al.*[67] prepared thin-film transistors (TFTs) by embedding $CsPbX_3$ (X = Br or I) quantum dots (QDs) into a-IGZO channels. The improved transfer efficiency of optical electrons from the quantum dots to the a-IGZO channels results in a high photoresponsivity exceeding 10^3 A W^{-1}, a detectivity of 10^{16} Jones, and a light-to-current ratio of 10^5 under visible light irradiation. Che *et al.*[96] developed a vertical field-effect phototransistor (VFEPT) using $CsPbBr_3$ nanocrystals (NCs) and a graphene electrode. The device features an ultra-short channel, which, combined with the high UV-visible light absorption of $CsPbBr_3$ NCs and the tunable Fermi level of graphene, results in high drain current densities of 0.25 A cm^{-2} for p-type and 0.2 A cm^{-2} for n-type conditions. Under 405 nm illumination with a power density of 342 mW cm^{-2}, the VFEPT achieves a responsivity of 2.2×10^3 A W^{-1}, a quantum efficiency of 6.7×10^5%, a detectivity of 1.1×10^9 Jones, as well as rise and decay times of 20 and 36 ms, respectively. Xie *et al.*[97] fabricated metal halide perovskite vertical field-effect transistors (MHP-VFETs) with the vertical field-effect transistor (VFET) structure. These MHP-VFETs are produced by a simple solution process with an MXene (TiC Tx) film as a perforated source electrode.

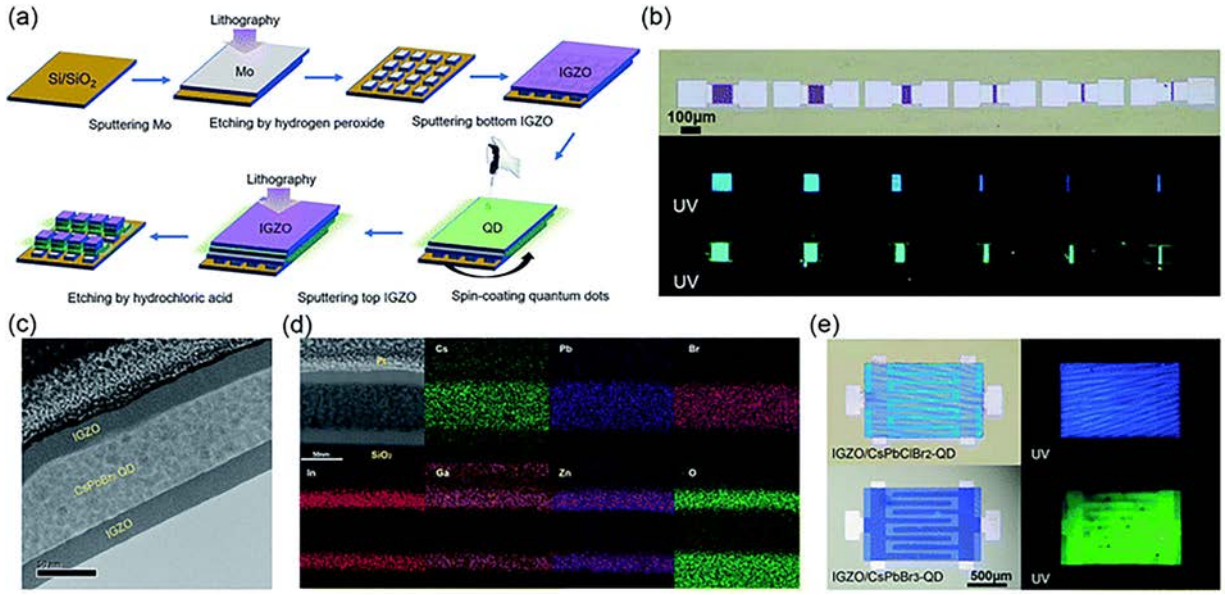

Fig. 9 (a) Fabrication of IGZO/QD TFT arrays by photolithography patterning; (b) optical microscopy images of IGZO/$CsPbClBr_2$-QD and IGZO/$CsPbBr_3$-QD phototransistor arrays under UV light irradiation (from left to right: devices with channel lengths varying from 100 to 12 μm); (c) TEM image of the cross-section of the channel region of the IGZO/$CsPbBr_3$-QD phototransistor; (d) EDS elemental maps of Cs, Pb, Br, In, Ga, Zn, and O in the channel region; (e) top view of the phototransistor in the synaptic response tests with interdigital electrodes.[92] (Reproduced from ref. 92 with permission from the Royal Society of Chemistry, copyright 2021.)

The MHP-VFETs show a high on/off ratio of up to 10^5 and a current density exceeding 6 mA cm^{-2} on account of the ultra-short channel lengths of the VFETs. Furthermore, the devices show an photoresponsivity of 2.1×10^3 A W^{-1} and a detectivity of 7.84×10^{15} Jones. Gao *et al.*[98] utilized a heterojunction phototransistor (HJPT) constructed by using a P-type OSC, poly[2,5-bis(3-tetradecylthiophen-2-yl)thieno[3,2-*b*]thiophene] (PBTTT or PBT), as the fast carrier transport pathway, $CsPbBrI_2$ perovskite quantum dots (PQD) as the efficient photosensitive layer, MoO_3 as the hole injection layer, and PLA as the electron trapping layer. Under illumination, the electrons generated by this transistor structure can be effectively captured by the polar polymer, while holes are rapidly extracted *via* the OSC, thereby achieving both high gain and fast carrier transport. The resulting HJPT exhibits superior photodetection performance, including a photosensitivity of 1.5×10^4, a photoresponsivity of 2.1×10^4 A W^{-1}, a detectivity of 1×10^{15} Jones, and a gain of 6.4×10^4 under weak incident light of 3 μW cm^{-2}. This device is suitable for visible light detection.

3.4. Photomultiplier photodetectors

A photomultiplier photodetector is a high-sensitivity photoelectric device based on the photoelectric effect and secondary electron emission (Fig. 10). This device can amplify weak light signals (even single photons) through multistage electron multiplication and output detectable electrical signals. The photomultiplier has high gain, low noise, and fast response, rendering it suitable for the detection of weak light. The photomultiplication effect involves the amplification of a single photoelectron signal millions of times through the cascade amplification mechanisms involving the external photoelectric effect (photoelectron emission) and secondary electron emission.

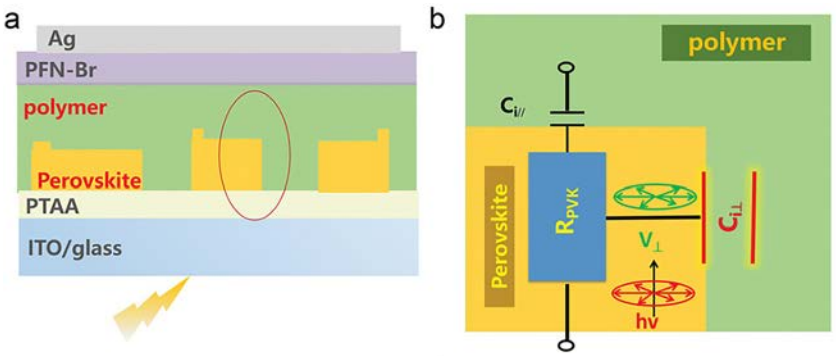

Fig. 10 (a) B-NPD photomultiplier detector structure with the circular ring marked as a typical 3D embedded part and (b) proposed equivalent circuit diagram of B-NPDs.[68] (Reproduced from ref. 68 with permission from the John Wiley and Sons, copyright 2023.)

The photoelectrons impinging onto a multistage multiplier pole generate an exponentially growing electron stream through secondary electron emissions, ultimately forming a detectable macroscopic current signal.

Su *et al.*[68] developed a broad/narrowband dual-mode photomultiplier photodetector that challenges the established application of chalcogenide single crystals for light multiplication in voltage-controlled broad/narrowband photodetectors. This microdevice consists of chalcogenide single crystals embedded in a conjugated polymer forming a 3D heterojunction structure. The heterojunction features a small radial capacitance that reduces the carrier burst and accelerates the carrier response. By tuning the applied bias direction, the device achieves an external quantum efficiency (EQE) of 300% to 1000% and a microsecond response in the range of 320 to 550 nm. Furthermore, the device provides a narrow-band response with a full-width at half-maximum (FWHM) of 20 nm. Tao *et al.*[99] have prepared photomultiplying perovskite photodetectors using a spin-bath-spinning technique in ambient air (Fig. 11). The deep trap states supplied by MoO_3 capture electrons generated in the active layer to facilitate hole tunneling injection through interface traps and create gains. The photomultiplier perovskite photodetector exhibits a high external quantum efficiency of over 52 800% and a rapid optical response time of approximately 18.5 μs. Fu *et al.*[100] fabricated a photomultiplier-type photodetector based on the $CH_3NH_3PbI_3$ perovskite. The properties are improved by introducing an appropriate intermediate layer to the $CH_3NH_3PbI_3$/electrode interface. The optimized device features an anode interface layer of

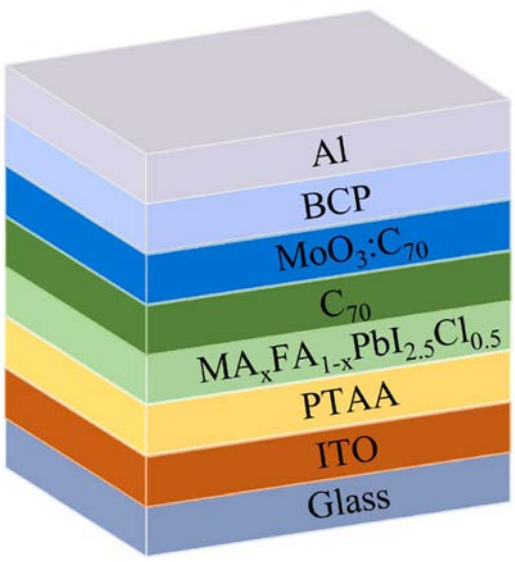

Fig. 11 Structure of the PM perovskite photodetector with ITO and Al as the anode and cathode, respectively, PTAA as a hole transport layer, and BCP as an electron transport layer (ETL)/hole blocking layer (HBL) with the aim of blocking hole injection from Al and suppressing the dark current. In $MA_xFA_{1-x}PbI_{2.5}Cl_{0.5}$, C_{70} is the electron transport layer (ETL) to suppress radiative complexation, while the MoO_3 layer supplies sufficient deep-state traps for multiplication.[99] (Reproduced from ref. 99 with permission from the Elsevier, copyright 2023.)

N,*N*′-di(naphthalene-1-yl)-*N*,*N*′-diphenyl-benzidine and a cathode interface layer of [6,6]-phenyl-C_{60}-methyl butyrate. The device shows a broadband response, photocurrent gain of approximately 177, detectivity of 4.6×10^{13} Jones, and improved response speed. Jeong *et al.*[101] developed a photomultiplier organic photodetector (OPD) by exploiting the ion migration properties of $CsPbI_3$ perovskite quantum dots (QDs). The OPD features a QD monolayer as the photogenerated middle layer and a donor–acceptor bulk heterojunction (BHJ) layer as the photoactive layer. Under irradiation, negative ions in the $CsPbI_3$ QDs migrate and accumulate near the interface between the QDs and the electrode, while producing hole injection from the electrode and a photomultiplier effect with an external quantum efficiency (EQE) exceeding 2000% at a 3 V bias. The PM OPD shows an EQ bandwidth product greater than 10^6 Hz and a −3 dB frequency of 125 kHz at 3 V. Zhang *et al.*[102] synthesized quantum-limited Sn^{2+}-doped $CsPb_{1-x}Sn_xBr_3$ nanocrystals by low-temperature thermal injection and created a trap-assisted photomultiplicative UV detector. The $CsPb_{0.966}Sn_{0.034}Br_3$ nanocrystal-based photodetector, operating at a reverse bias of −7 V, exhibits wavelength-dependent detection with a specific detectivity of 10^{11} Jones for ultraviolet light between 310 and 400 nm. This photodetector shows an EQE of approximately 1940% at 340 nm, reflecting substantial gain under large reverse bias conditions. Jagadeeswararao *et al.*[103] optimized hole trap states in lead-free $Cs_{1.98}AgBi_{1.15}Br_{7.9}$ double perovskite (DP) by adjusting the composition to slightly enrich Bi and highly enrich Br. The device has an ITO/SnO_2/$Cs_{1.98}AgBi_{1.15}Br_{7.9}$/poly(3-hexylthiophene) (P3HT)/MoO_x/Ag diode structure, with SnO_2 and P3HT layers serving as hole and electron barrier layers, respectively. It exhibits a high EQE of nearly 16 000%, a responsivity of 50 A W^{-1}, and a specific detectivity exceeding 10^{12} Jones at −3 V. Ishii *et al.*[104] hybridized a molecular layer of the organic europium (Eu) complex with halide perovskite ($MAPbI_3$) nanocrystals to control charge transport between the photoexcited perovskite and the metal electrode. The accumulation of holes in photoexcited perovskite nanoparticles, combined with charge tunneling through Eu complex molecules, results in an efficient photomultiplicative reaction. The photodetection device composed of the Eu complex and perovskite absorber generates a big photo-induced current under weak monochromatic illumination (<1 mW cm^{-2}), giving rise to a quantum conversion efficiency of 29 000% and a power responsivity of 1289 A W^{-1}. Enhanced optical detection is accomplished by employing perovskite nanoparticles (<5 nm) with a large surface area in contact with the Eu complex. Kang *et al.*[105] demonstrated that $CsPbBr_3$ perovskite nanocrystals (NCs) can enhance the properties of photomultiplier organic photodiodes (PM-OPDs). The ion-polarized $CsPbBr_3$ NCs are uniformly distributed throughout the depletion region of the Schottky junction interface to stabilize trapped electrons. The optimized $CsPbBr_3$-NC-embedded poly(3-hexylthiophene-binary) PM-OPD exhibits an exceptionally high external quantum efficiency of 2 840 000%, a specific detectivity of 3.97×10^{15} Jones, and gain-bandwidth product of 2.14×10^7 Hz. Kim *et al.*[106] prepared electrospun trication perovskite fibers permeated with hole-transporting

π-conjugated small molecules such as 2,2′,7,7,7′-pentamethyl-9,9-dimethylspiro[fluorene-9,9′-xanthene] (spiro-OMeTAD). The high density of charge traps on the surface of the electrospun fibers facilitates photomultiplication and allows light-generated holes to traverse the active layer multiple times before recombining with the trapped electrons. The hybrid perovskite photodetector operating at a low bias of 5 V shows the high gain and external quantum efficiency (EQE) of up to 3009%, which decreases slightly to about 2770% after 3 months in the air.

4. Applications of perovskite photodetectors

Perovskite photodetectors have garnered widespread attention because of their outstanding properties in various fields, such as imaging sensing, optical communication, flexible electronics, and spectral detection.[107–110]

4.1. Image sensing

Perovskite photodetectors are promising in image sensing because of their outstanding characteristics and versatility. The perovskite photodetector in an image sensor converts the optical signal into an electrical signal with good spatial resolution with the aid of a pixel array. Sun *et al.*[111] developed a perovskite photodetector (PP-PD) using a model space limitation method that combines polarization sensitivity with excellent photoelectric properties. The detector shows not only outstanding photoelectric conversion but also a high polarization sensitivity with a on/off ratio of 3.4×10^4, low dark current of 1.56×10^{-11} A, and rapid response time. The responsivity reaches 10.6 A W^{-1}, and the detectivity is 3×10^{12} Jones. Polarization tomography sensing is accomplished by the stepwise scanning of the device. Li *et al.*[112] utilized modified lithography to create perovskite microchip arrays for an integrated photodetector (PD) array based on these microchips. The PD array exhibits notable optical response at zero bias, a on/off ratio of 1.5×10^4, responsivity of 0.38 A W^{-1}, and specific detectivity of 1.7×10^{12} Jones. The array, which also shows good uniformity and minimal variation between pixels, can capture light tracks in real time with high resolution. Zhang *et al.*[113] deposited $MAPbI_3$ perovskite films onto a patterned SiO_2/Si substrate and assembled them into an 8×8 photodetector array. The $MAPbI_3$ perovskite/Si heterojunction photodetector exhibits a responsivity of 18.4 mA W^{-1}, a specific detectivity of 1.8×10^{12} Jones, and an I_{light}/I_{dark} ratio of 295. The electrical analysis reveals that the photodetector array, which has excellent uniformity and repeatability, can record 'H' images generated during 970 nm light exposure. Zhao *et al.*[114] employed a Lewis base and a thionacetamide additive to passivate defects in $CsPbBr_3$ perovskite films *via* Lewis acid–base interactions. The device shows a dark current density of 4.01 nA cm^{-2}, a peak responsivity of 0.39 A W^{-1}, rapid rise and decay times of 12.4 and 56.2 μs, respectively, a peak detectivity of 1.08×10^{13} Jones, and a linear dynamic range of 99 dB, which significantly outperform $CsPbBr_3$ perovskite photodetectors without TAA additives. This device excels in high-resolution imaging at zero bias. Xia *et al.*[115] developed a flexible photodetector by fabricating a methylamine lead-iodine/graphene heterojunction using two-step chemical vapor deposition using high-quality graphene film as the template. The photodetector exhibits a photoresponsivity of 10^7 A W^{-1}. The inclusion of graphene suppresses the recombination of electron–hole pairs and enhances the photocurrent of the device. The flexible photodetector array (24×24) image sensor that emulates the functions of cones in the retina has shape recognition and color discrimination capabilities (Fig. 12). He *et al.*[116] used low-temperature gas-phase synthesis and self-limiting chemical vapor deposition to prepare ultrathin perovskite materials with a 2D thickness, a lateral size of 1.5×1.5 cm, and good stability. The photodetector made of these materials shows impressive responsivity (3.7×10^3 A W^{-1}), a fast response time (<10 μs), and excellent low-illumination image sensing characteristics. Wang *et al.*[117] conducted patterned growth on an addressable perovskite photodetector array by a solution method facilitated by uncured polydimethylsiloxane (PDMS) oligomers. This technique produces an $MAPbI_3$ thin-film photodetector array with minimal inter-pixel variation, a responsivity of 2.83 A W^{-1}, a specific detectivity of 5.4×10^{12} Jones, and rapid response times (52.7/57.1 μs for response/recovery). The 8×8 addressable photodetector array with adequate spatial resolution is fabricated for real-time image sensing. Oh, *et al.*[118] incorporated metal ions into thin inorganic $CsPbBr_3$ perovskite films using metal–organic framework nanoparticles. The Zn^{2+} ions passivate the uncoordinated defects in the defective perovskite crystals to enhance the environmental stability and photoluminescence, resulting in a quantum yield of about 14%. The thin Zn-doped $CsPbBr_3$ film maintains nearly 90% of the initial photocurrent at 60% RH after 15 days. Moreover, the sensor is capable of visually programming images based on both the photocurrent and photoluminescence, thus serving as a dual-mode image sensor.

Perovskite photodetectors are spurring the advance of image-sensing technology for higher resolution, lower power consumption, and wider applications through efficient photoelectrical conversion, wide spectral response, and flexible design. Combining silicon-based complementary metal–oxide semiconductors (CMOS) and flexible electronics technology is expected to spur the development of medical devices, autonomous driving, consumer electronics, and other commercial products.

4.2. Optical communication

Perovskite photodetectors, known for their high sensitivity, wide spectral response, fast response time, and low noise, offer significant advantages in optical communication systems. When an optical signal (such as a fiber or free-space laser) illuminates the perovskite active layer, photons are absorbed to excite electron–hole pairs, which are subsequently driven by the built-in electric field) or applied bias. The carriers separate rapidly and migrate to the electrodes to form a photocurrent.

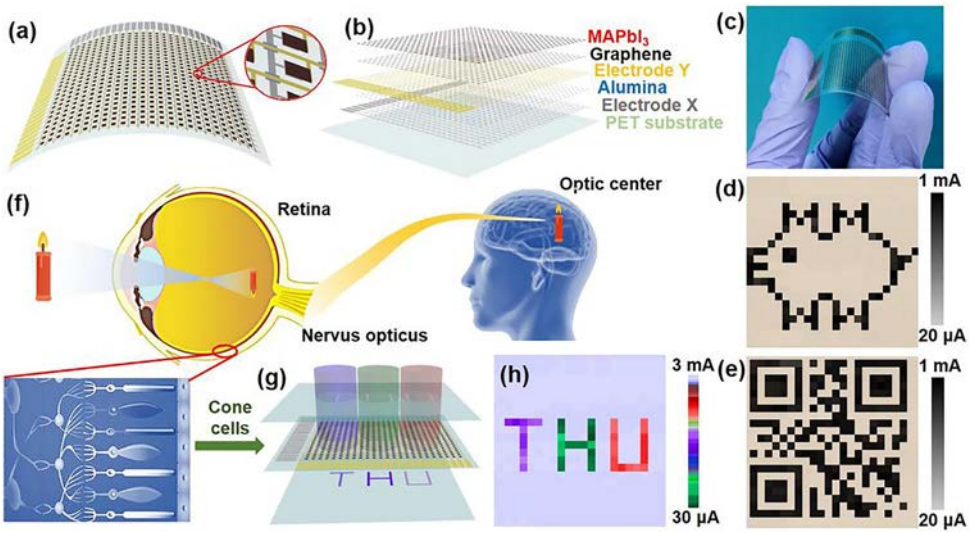

Fig. 12 Preparation of the flexible image sensor with the vdWs $MAPbI_3$/graphene heterostructure for image recognition: (a) and (b) schematic illustration of the flexible (24 × 24) pixels image sensor on a PET substrate; (c) photograph of the flexible image sensor; (d) and (e) output images of a cartoon pig in (d) and QR code of a 'photodetector' in (e) under light illumination (30 μW, 633 nm); (f) schematic illustration of the multicolor imaging systems in a human visual system; (g) schematic of the image sensor with the vdWs $MAPbI_3$/graphene heterostructure as cone cells; (h) output image of the flexible image sensor under different light illumination (75 μW, 380 nm, 633 nm, and 750 nm).[115] (Reproduced from ref. 115 with permission from the Elsevier, copyright 2020.)

By optimizing the perovskite components and device structure, the carrier transit time and RC delay can be reduced to satisfy the requirements of high-speed communication such as high-speed data transmission, multi-wavelength signal detection, and quantum communication. Wang *et al.*[119] developed $MAPbI_3$-based photodetectors with a p–i–n structure showing responsivity of 0.4 A W^{-1}, a response time of 7.58 μs, and an on/off current ratio of 2.0 × 10^5. The modified unpackaged photodetectors exhibit excellent long-term environmental stability (>100 days) under ambient conditions and can be integrated into visible optical communication systems to transmit ASCII-encoded information as an optical signal receiver (Fig. 13). Liu *et al.*[120] prepared a Bi_2O_3 layered, band-resolved perovskite photodetector with features such as self-powering, dual-sided response, and high sensitivity for both short and long-wave ultraviolet and visible signals. The device functions well without an external bias and achieves peak responsivities of 42.1 and 72.3 mA W^{-1} during front and rear illumination, respectively. The photodetector is suitable for optical communication and encryption applications as it enables reversible message transfer through the conversion and decoding of illumination modes and binary numbers. With 8 radiation combinations and a 10-bit command key, it supports over 1 billion encryption methods. He *et al.*[121] introduced metasurfaces made from hybrid organic–inorganic perovskites (HOIPs) to enhance broadband absorption and photon-to-electron conversion. The broadband photodetector based on HOIP metasurfaces shows a photocurrent increase of more than 10 times in the UV-to-visible light spectrum. The device features a response time of less than 5.1 μs at wavelengths of 380 532, and 710 nm with a 3 dB bandwidth greater than 0.26 MHz. This photodetector can serve as a signal receiver to transmit 2D color images in broadband optical communication. Cheng *et al.*[122] have developed 2D perovskite $FA_3Bi_2I_9$ by incorporating a Sn–Pb mixed perovskite precursor solution with bismuth iodide (BiI_3). Under visible and near-infrared (NIR) light irradiation, the film generates more carriers at the bottom and top, thus facilitating easier electron separation and transmission to the respective electrodes as well as both negative and positive polarity responses. The device hides the positive NIR signal with the negative visible light signal by using the positive NIR signal as the effective signal and the negative visible light as the interference signal. Chen *et al.*[123] developed a perovskite heterojunction with $(CmH_{2m+1}NH_3)_2PbI_4$/$MAPbI_3$ (m = 4–8) and $(CmH_{2m+1}NH_3)_2PbI_4$/$MAPbI_3$ (m = 2–8) to produce a filter-free band-pass photodetector showing a near-square optical response. The strong and sharp exciton absorption of 2D perovskite results in a narrow response starting width of 10 ± 1 nm. In addition, intense photoluminescence (PL) self-absorption by the 2D perovskite minimizes PL leakage from the primary absorber to the secondary photoactive zone. By integrating bromine-based 2D/3D perovskite photodetectors, the system achieves a low spectral crosstalk and a wavelength discrimination starting edge of approximately 20 nm. Liu *et al.*[124] have used a p-type doping strategy with copper ions for perovskite films to improve the pore conductivity, passivate trap states, prevent charge accumulation, and reduce photogenerated carrier recombination. The device shows a maximum responsivities of 0.37 A W^{-1}, a detectivity of 1.06 × 10^{12} Jones, a linear dynamic range exceeding 101 dB, and an optical response speed close to 5 μs. By integrating into an optical communication system, the perovskite photodetector serves as an optical signal receiver for digital signal transmission, consequently enabling accurate character transmission and high-fidelity audio signal recovery.

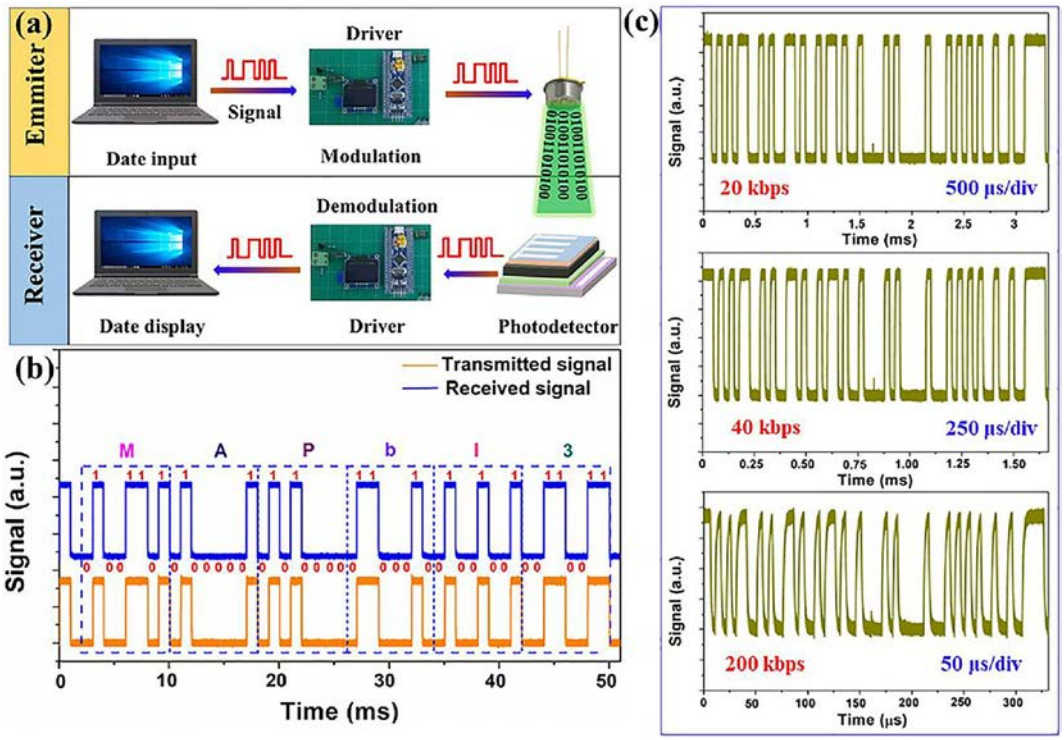

Fig. 13 (a) Schematic of the visible light communication system; (b) electrical signal waveform obtained from the single-chip processor and PDs; (c) digital data waveform received by devices at different transmission rates.[119] (Reproduced from ref. 119 with permission from the Elsevier, copyright 2024.)

Yan *et al.*[125] utilized 2D oxide perovskites to design an inorganic–organic heterojunction that fills pinholes in the nanosheet film and suppresses dark currents by 100 000 times. The heterojunction accelerates charge carrier transport, giving rise to a fast rise response time of 0.7 ms and decay response time of 8.5 ms. In addition, it exhibits excellent self-supply characteristics and high responsivity of 60 mA W^{-1}. The photodetector has a detection angle of 30° and can communicate effectively over a short distance of 1.2 m in UV-optical communication systems.

Perovskite photodetectors provide a low-cost and high-performance solution for optical communication systems due to their high-speed responses, wide spectral coverages, and integrability. By optimizing the carrier dynamics and device structure, high-fidelity conversion of optical signals can be realized. On the heels of the recent advances in materials engineering and device technology, perovskites are expected to be more widely used in optical fiber communication, optical integration, and free-space communication.

4.3. Flexible devices

Perovskites are increasingly recognized for their potential in flexible photodetectors due to their mechanical flexibility, low cost, and compatibility with low-temperature processing. Furthermore, they are suitable for flexible substrates, such as polymers, carbon cloths, fibers, paper, soft electrodes (including metal-based conductive networks), carbon-based materials, and 2D materials. The remarkable photoelectric properties, ease of cryogenic solution preparation, and adaptability to flexible substrates have made perovskite photodetectors a focal point in the development of flexible devices. Jing *et al.*[126] developed a flexible photodetector by using ultra-thin single-crystal perovskite films as the active layer. The device shows a responsivity of 5600 A W^{-1} when the film thickness is reduced to 20 nm. Despite undergoing thousands of bending cycles, the photodetector maintains good photoelectric properties as demonstrated by high-speed photoelectric detection with a 0.2 MHz 3 dB bandwidth. Xu *et al.*[127] prepared cost-effective transparent $SrVO_3$ conductive oxide (TCO) thin films on a flexible mica substrate to form transparent, flexible, and self-powered perovskite photodetectors. These devices, which require no external power supply, exhibit a high responsivity of 42.5 mA W^{-1}, rapid rise and decay times of 3.09 ms and 1.23 ms, respectively, as well as excellent flexibility. They remain stable after dozens of 0° bending and retain optical transparency and conductivity even after 10^5 bending cycles. Marunchenko *et al.*[128] fabricated responsive and flexible photodetectors using cesium tribromide lead ($CsPbBr_3$) and single-wall carbon nanotube (SWCNT) microcrystals as electrodes. The flexible perovskite photodetector shows a responsivity of 1321 A W^{-1} at 5 V and excellent properties at 505 nm and 1 mW cm^{-2}. The SWCNT films provide stability for 10^4 bending cycles while maintaining all the parameters for at least 1.5 months under ambient conditions. Wang *et al.*[129] prepared flexible $CH_3NH_3PbI_3$ perovskite thin films by dual-source physical vapor deposition and brush coating on paper substrates. Both methods produce photodetectors with similar photodetection capabilities and reproducibility, including an initial photocurrent retention of up to 75% after 500 bending cycles as well as good flexibility and stability. The 6 × 6 perovskite

photodetector array based on scalable origami exhibits excellent full spectral acquisition capabilities and has large potential in 3D photoelectric detection. Yang *et al.*[83] utilized $Pb(SCN)_2$ as a lead source to prepare high-quality $MAPbI_3$ films and combined them with 1D ferroelectric perovskite $TMIMPbI_3$ to create self-powered, flexible, and stable photodetectors featuring enhanced ferrothermal optoelectronic effects due to the heterojunction. The photodetectors have improved photoelectric characteristics such as a dark current of 7×10^{-9} A, responsivity of 6.6 mA W^{-1}, and detectivity of 5×10^9 Jones. They also have excellent folding durability and moisture stability. Saraf *et al.*[130] prepared a porous polystyrene–perovskite composite film using a single-step process to fabricate a highly flexible, stable, and large-area (3 cm^2) photodetector. The device retains 85% of its original optical current after 10 000 bending cycles at 120° and boasts a responsivity of 2.73 A W^{-1}, a detectivity of 6.2×10^{13} Jones, and a high switching ratio of 1×10^4 besides remarkable stability under the combined stress imposed by moisture, ambient air, and indoor light, resulting in 92% retention after 30 days (Fig. 14). Kim *et al.*[131] prepared a flexible photodetector with polarization sensitivity by accurately aligning perovskite nanowires (NWs). The alignment is enhanced by brushing the nanowires with a toluene-dispersion solution. The degree of alignment impacts the photodetector, as well-aligned nanowire photodetectors exhibit a current response twice that in the polarization direction. Consequently, the device retains 80% of the photoelectric detection characteristics after 500 bending cycles. Zhan *et al.*[132] fabricated flexible perovskite films using anti-solvent-assisted polymer self-coating and in-crystallization printing technology, resulting in a 'brick structure' akin to nacre layers by bonding perovskite particles with the polymer. Combining a hemispherical grating (HG) with a porous photonic crystal (PC) (HG-PC) improves the crystal quality and light capture capability. The flexible HG-PC photodetector shows a responsivity of 17.31 A W^{-1} and a detectivity of 5.02×10^{13} Jones. Moreover, it retains 95% of its initial photocurrent after 1000 bending cycles with a 2 mm radius of curvature.

4.4. Spectral detection

The bandgap tunability of perovskite materials enables them to cover a broad spectral range from UV to infrared. Through bandgap tunability and efficient optoelectrical conversion, optical signals of different wavelengths are converted into distinguishable electrical signals and combined with array design and algorithm analysis. Hence, high-resolution and low-cost spectral detection can be attained for spectral detection by perovskite photodetectors. Zhang *et al.*[110] have extended the spectral response of perovskite photodetectors to the solar-blind UV region by phosphor encapsulation. By overlaying a three-color phosphor with a high photoluminescence quantum yield, incident UV light is converted into visible light, leading to an external quantum efficiency of 12.13% at 265 nm with no

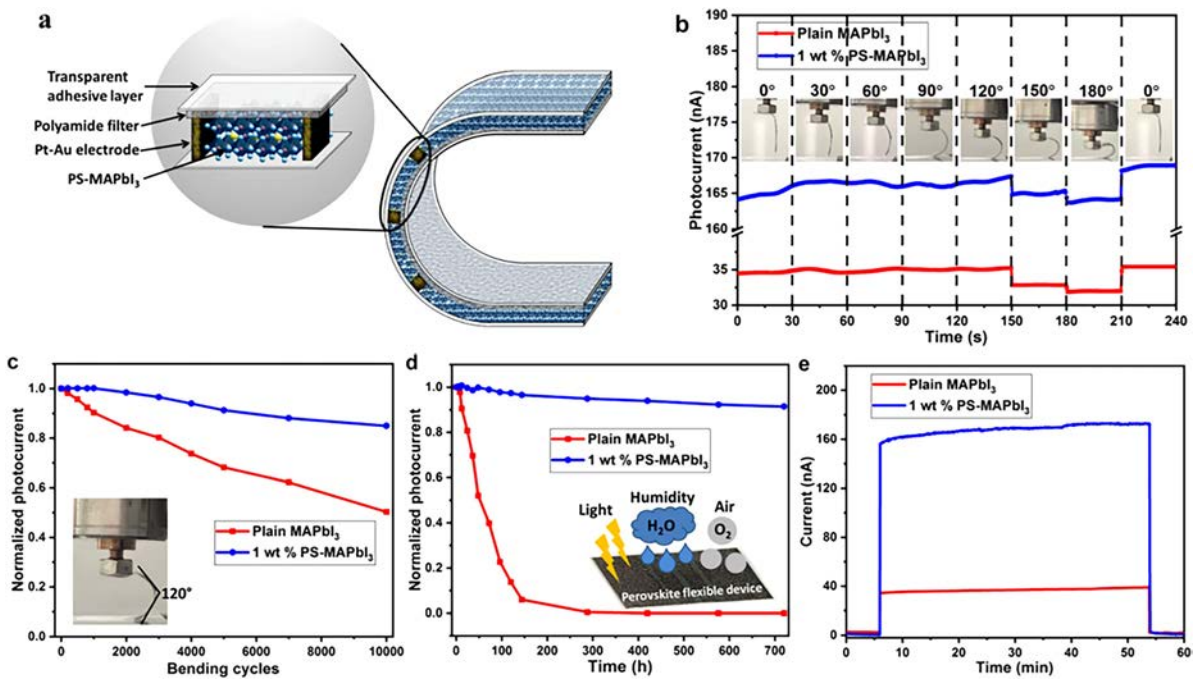

Fig. 14 (a) Schematic showing the bending of the flexible PS-$MAPbI_3$ photodetector; (b) photocurrent response of the plain $MAPbI_3$ and 1 wt% PS-$MAPbI_3$ devices under 650 nm light illumination at an intensity of 0.1 mW cm^{-2} during the bending process with the inset showing the corresponding optical images of the device at different bending angles; (c) normalized photocurrents of the flexible devices after different bending cycles at 120°, demonstrating the mechanical stability and durability of the 1 wt% PS-$MAPbI_3$ device after 10 000 bending cycles; (d) normalized photocurrents of the devices with an adhesive layer after aging continuously in ambient air, 35–40% relative humidity, and under room light for 720 hours (30 days); (e) operational stability of the devices at a constant bias of 2 V under 650 nm light irradiation with an intensity of 0.1 mW cm^{-2}. The measurements are carried out on multiple devices (at least 4) and yield an error range of 3–5% for all samples.[130] (Reproduced from ref. 130 with permission from the Springer Nature, copyright 2020.)

bias and an initial response close to zero. The spectral responsivity and detectivity are 0.0269 A W^{-1} and 7.5 × 10^{11} Jones, respectively. Moreover, the device exhibits a large linear dynamic range of 105 dB, a fast response time (50.16/51.99 μs), and excellent stability. Wang *et al.*[133] developed a filter-free, self-driven perovskite narrow-band photodetector (PNPD) based on the defect-assisted charge collection narrow-band (CCN) mechanism. By tuning the halide composition of the perovskite layer, the bandgap can be adjusted to accomplish broad spectral responses from red to near-infrared (NIR) with an FWHM of less than 30 nm. The photodetector shows a detection peak at 800 nm, low noise current of 0.02 pA $Hz^{-1/2}$, specific detectivity of 1.27 × 10^{12} Jones, and fast response speed with rise/fall times of 12.7/6.9 μs (Fig. 15). Xue *et al.*[134] enhanced the spectral selectivity and detection properties by doping with Bi^{3+} and incorporating surface recombination to suppress photocarriers generated by short-wavelength light excitation. The narrowband photodetectors featuring a PN heterojunction achieve a narrow FWHM of 7.7 nm, a specific detectivity of 1.5 × 10^{10} Jones, as well as rapid response and fall times of 8 and 137 μs, respectively. Mei *et al.*[135] fabricated photodetectors capable of simultaneous UV-visible-short-wavelength infrared (SWIR) detection using single-crystal $MAPbBr_3$ nanoplates. The nanoplate photodetectors (NPDs) have a high external quantum efficiency (EQE), of 1200%, a specific detectivity of 5.37 × 10^{12} Jones, and a rise time of 80 μs. The NPDs perform well in the near-infrared and SWIR spectral regions (850–1450 nm). Unencapsulated devices retain good UV laser irradiation durability and maintain periodicity and repeatability for 29 days under atmospheric conditions. Zuo *et al.*[136] have developed lead perovskite films with gradients of $MAPbCl_3$–$MAPbBr_3$ and $MAPbBr_3$–$MAPbI_3$ through self-diffusion and mutual diffusion of solutions. These films exhibit a photoabsorption range of 410–781 nm. By using these gradient bandgap films, the self-powered multiband photodetectors show varied spectral responses at different locations without the need for an applied bias voltage. Zhang *et al.*[137] prepared two-dimensional perovskite $NdNb_2O_7$ (NNO) nanosheets by solid-state calcination and liquid-phase exfoliation. The single NNO nanosheet photodetector (PD) can detect UV light (260 nm, 3 V) with a responsivity of 62 A W^{-1}, high detectivity (6.7 × 10^{12} Jones), and high spectral selectivity (R_{260}/R_{400} = 9000). It also shows a rapid response time (0.1 ms rise time and 7.8 ms fall time) and long-term stability. Wang *et al.*[138] synthesized lead-free perovskite $CsSnX_3$ (X = Cl, Cl/Br, Br) quantum dots and tuned the spectral properties by altering the anion compositions. The quantum dots are used to construct a sensitive UV light detector with good deep-UV sensitivity. Due to the small defect density of the $CsSnBr_3$ quantum dots, the device achieves a specific detectivity (D^*) of up to 1.27 × 10^{11} Jones at 365 nm.

Perovskite photodetectors can be used for spectral detection on account of the adjustable bandgap and high efficiency photoelectrical conversion. By adjusting the composition of perovskite, the bandgap can be regulated to selectively absorb photons of specific wavelengths and convert them into

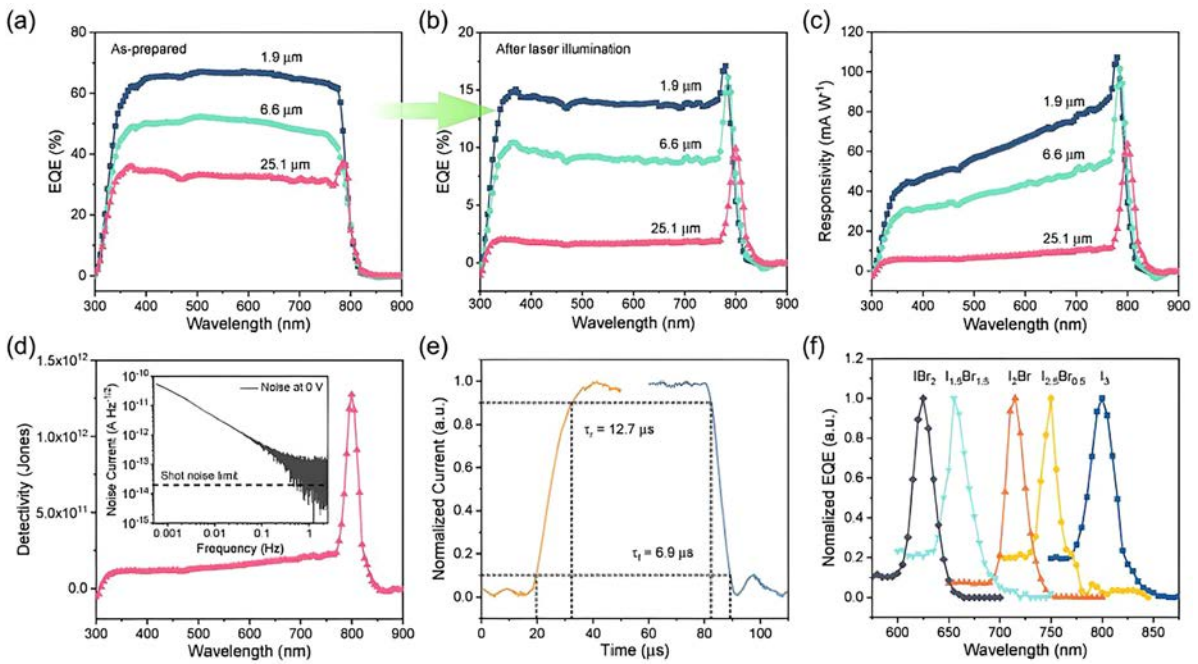

Fig. 15 Properties of self-driven PNPDs: (a) EQE spectra of $MAPbI_3$ photodetectors composed of perovskite layers with various thicknesses; (b) EQE spectra after laser illumination; (c) responsivity spectra calculated from EQE; (d) specific detectivity spectra of $MAPbI_3$ photodetectors with a perovskite layer thickness of 25.1 μm (inset: total noise current and shot noise limit); (e) response time of the $MAPbI_3$ narrowband photodetector; (f) normalized EQE spectra of the PNPDs with various halide compositions. All the measurements are conducted without an external bias.[133] (Reproduced from ref. 133 with permission from the John Wiley and Sons, copyright 2020.)

electrical signals. Combined with an array design, multi-spectral resolution, and rapid analysis can be realized for environmental monitoring (pollutant identification), biomedical and agricultural detection, and other fields.

4.5. Other applications

Perovskite photodetectors have many applications in other fields. For example, Wang *et al.*[39] have synthesized $CsCu_2I_3$ single crystals for X-ray detectors. The sensitivity of the $CsCu_2I_3$ single crystal X-ray detector is 424 μC Gy_{air}^{-1} cm^{-2}, and the lowest detectable X-ray dose rate is 0.93 nGy s^{-1}. Dong *et al.*[139] designed a micro-nano X-ray detector based on an all-inorganic lead-free $CsAg_2I_3$ (CAI) single-crystal microstrip. The photodetector has a response rate of 23.59 mA W^{-1}, a detection rate of 10^{10} Jones, and a fast response. In X-ray detection, the sensitivity is as high as 515.49 μC Gy_{air}^{-1} cm^{-2}, and the detection limit is as low as 14.65 μC Gy_{air}^{-1} together with excellent operational stability and excellent long-term stability. Gao *et al.*[140] fabricated heterojunctions by employing p-type polymer semiconductors (PDPPBTT) and $CsPbBrI_2$ perovskite nanocrystals as the conduction channels and photoconductors, respectively. They further developed a top-gate heterojunction phototransistor for X-ray detection. This device exhibits a high-gain mechanism and flexibility, achieving an ultra-high sensitivity of over 10^5 μC Gy_{air}^{-1} cm^{-2}. Notably, it remains capable of effectively detecting X-ray signals even at an extremely low dose rate of 1 nGy_{air} s^{-1}, while offering a spatial resolution of up to 11.2 line pairs per millimeter (lp mm^{-1}). Cao *et al.*[141] designed a heterostructure integrating indium gallium zinc oxide (IGZO) as the transistor channel and $CsPbI_2Br$ perovskite nanocrystals as the X-ray active material. This structure was utilized to construct an X-ray phototransistor for direct X-ray detection. The detector demonstrates remarkable performance with a sensitivity exceeding 10^6 μC Gy_{air}^{-1} cm^{-2} and a detection limit as low as 3 μGy_{air}^{-1}. Furthermore, it achieves an excellent balance between high sensitivity, low detection limit, flexibility, high imaging resolution, lightweight design, and cost-effectiveness. Xia *et al.*[142] successfully synthesized a series of post-perovskite semiconductors with densities exceeding 5 g cm^{-3} by utilizing shared edge-face connections of octahedra and strong polarization between metal ions and sulfide ions. These dense materials exhibit superior electrical transport properties while retaining semiconductor characteristics, making them suitable for hard X-ray detection. Specifically, the $BiCuSCl_2$ post-perovskite detector demonstrates a high sensitivity of 4126 μC Gy_{air}^{-1} cm^{-2} and an ultra-low detection limit of 4.3 nGy_{air} s^{-1}. Liu *et al.*[143] developed organic–inorganic hybrid antiperovskites ($(2\text{-Habch})_3Cl(PtI_6)$) featuring indirect band transitions and low orbital symmetry at the band edges. This structure enables an exceptionally long carrier lifetime exceeding 3 milliseconds. Moreover, the X-ray detector based on $(2\text{-Habch})_3Cl(PtI_6)$ achieves an ultra-low dark current of 0.21 nA cm^{-2} at a bias voltage of −1 V, a high sensitivity of 1.0×10^4 μC Gy_{air}^{-1} cm^{-2}, an ultra-low detection limit of 2.4 nGy_{air} s^{-1}, and excellent operational stability. Wang *et al.*[144] exploited the presence of excessive volatile $PbBr_2$ in $CsPbBr_3$ films to lower the melting point and promote recrystallization at temperatures significantly below its melting point. The resulting X-ray detector based on the dense non-stoichiometric $CsPbBr_3$ thin film exhibits a high sensitivity of 4.24×10^4 μC Gy_{air}^{-1} cm^{-2} and a low detection limit of 136 nGy_{air} s^{-1}, enabling real-time dynamic X-ray imaging. Chen *et al.*[145] prepared quasi-two-dimensional Ruddlesden–Popper (RP) phase perovskites, particularly the thick film of $PEA_2MA_4Pb_5I_{16}$, using the carbonyl array collaborative crystallization (CSC) strategy. The $PEA_2MA_4Pb_5I_{16}$ RP perovskite X-ray detector based on the CSC strategy shows high sensitivity (reaching 236 μC Gy_{air}^{-1} cm^{-2} at 30 V), a low detection limit (22.7 nGy_{air} s^{-1}), and excellent operational stability. Liang *et al.*[146] achieved stable and less toxic two-dimensional perovskite single crystals (SCs) through interlayer spacing engineering combined with a self-balancing strategy. The X-ray detector based on $(PEA)_2Ge_{0.5}Pb_{0.5}I_4$ single crystal exhibits a high sensitivity of 13488 μC Gy_{air}^{-1} cm^{-2}, a low detection limit of 8.23 nGy s^{-1}, and a high spatial resolution of 8.56 lp mm^{-1}. Song *et al.*[147] grew DABCO-NH_4Br_3 single crystals from aqueous solutions *via* the slow cooling method. These single crystals possess a large half-gap of approximately 16 eV. The X-ray detector based on DABCO-NH_4Br_3 single crystals achieves a sensitivity of up to 173 μC Gy_{air}^{-1} cm^{-2} and a detection limit of 4.96 μC Gy_{air} s^{-1}. The DABCO-NH_4Br_3 single crystal detector is capable of clear imaging with high resolution and contrast. Han *et al.*[148] used solution-treated $PEA_2MA_4(Sn_{0.5}Pb_{0.5})_5I_{16}$ polycrystalline films as photoactive layers to detect polarized photons from 300–1050 nm. The photodetector shows a polarization ratio of 0.41 at 900 nm and a dichroic ratio (I_{max}/I_{min}) of 2.4. With a response width of 900 kHz, I_{on}/I_{off} ratio of approximately 3×10^8, linear dynamic range of 0.15 nW to 12 mW, noise current of 8.28×10^{-13} A × $Hz^{-0.5}$, specific detectivity of 1.53×10^{12} Jones, weak signal sensing and imaging with high resolution and speed are accomplishable and such photodetectors can also be used for target recognition. Cao *et al.*[149] fabricated a light-stimulated synaptic device (photonic synapse) based on perovskite/In–Ga–Zn–O heterojunction phototransistors. The combination of high-efficiency light absorbers, high-mobility channels and heterojunction device structures provides this light-stimulated synapse with efficient photon-to-electron conversion and an inherent high-gain mechanism. High-performance photonic synapses have the basic functions of excitatory postsynaptic current (EPSC), paired impulse promotion (PPF), and short-term memory-to-long-term memory conversion (STM-LTM). This transistor has ultra-sensitive light detection, so that the light power consumption of this photonic artificial synapse can be as low as 2.6 picojoules, with extremely high energy efficiency.

5. Conclusion and outlook

Due to the excellent optical and electrical properties of perovskite materials, perovskite photodetectors have rapidly become one of the hot areas in optoelectronics research. The perovskite carrier dynamics is crucial to the performance of

photodetectors. A deeper understanding of the carrier generation, migration, and recombination processes can guide materials selection, fabrication processes, and device design to improve the response speed, sensitivity, stability, and overall performance of photodetectors and to promote more widespread applications of perovskite photodetectors. This review describes the mechanisms of carrier generation, migration, and recombination in perovskite materials, the effects of the perovskite microstructures on carrier behavior and stability, and the application of time-resolved spectroscopy techniques to the investigation of carrier dynamics. The working principles and current research status of photoconductive, photovoltaic, phototransistor, and photomultiplier-type perovskite photodetectors, as well as their applications in various fields, are reviewed. Finally, future developments and prospects are discussed.

Although the optoelectronic properties of perovskite materials have been improved and they have great potential in photodetectors, several challenges still need to be addressed:

(1) Perovskite materials face environmental stability issues during long-term use, particularly regarding the sensitivity to moisture, oxygen, and light. Moisture, oxygen, and ultraviolet (UV) light exposure can degrade perovskite materials to compromise their performance. Instability limits the reliability of perovskite materials in practical applications. Hence, maintaining the high energy-conversion efficiency and long-term stability of perovskite materials under various environmental conditions is imperative. Future research should focus on the development of surface passivation and interface engineering to address stability issues, for example, by introducing hydrophobic polymer passivation layers to protect perovskite surfaces from defects or adding appropriate interface layers between the perovskite and electrodes to reduce exposure to moisture and oxygen.

(2) Crystal defects in perovskite materials are the key factors affecting the optoelectronic properties. Crystal defects often lead to carrier recombination, reduced mobility, and a slower photodetector response. The defects in perovskite materials include point defects, dislocations, vacancies, and impurities. These defects affect not only the stability of perovskite materials but also their optoelectronic properties. Optimizing the fabrication process to improve crystal quality and reduce defects is crucial to mitigating the impact of crystal defects and grain boundaries on the optoelectronic characteristics. The use of defect passivation agents to repair surface and grain boundary defects, along with doping and interface engineering, can stabilize the crystal structure and reduce the effects of grain boundaries.

(3) Perovskite materials have good absorption properties in the visible light range. However, broadening the response range to ultraviolet (UV) and near-infrared (NIR) presents several challenges. The spectral response range of perovskite materials is limited by their band structures. Tuning the band structure to absorb a broader spectrum remains a key area of research. Future strategies to expand the absorption range include modifying the chemical composition of perovskite materials, introducing different doping elements, and incorporating perovskites with other light-absorbing materials.

Data availability

No primary research results, software, or code have been included, and no new data were generated or analyzed as part of this review.

Conflicts of interest

There are no conflicts to declare.

Acknowledgements

This work was supported by the National Natural Science Foundation of China (12474433 & 11974371), the Key Area Funds of Universities of Guangdong Province (2023ZDZX1021), Shenzhen Science and Technology Research Funding (JCYJ20220818101412027 & JCYJ20241202124900002), the Scientific Research Start-Up Fund of Shenzhen Technology University (GDRC202140), and the City University of Hong Kong Donation Research Grants (DON-RMG No. 9229021 and 9220061).

References

1 P. Vashishtha, R. Tanwar, P. Prajapat, A. K. Gangwar, L. Goswami, P. Singh, J. Tawale, N. Dilawar and G. Gupta, *J. Alloys Compd.*, 2023, **948**, 169735.
2 T. Yan, Z. Li, L. Su, L. Wu and X. Fang, *Adv. Funct. Mater.*, 2023, **33**, 2302746.
3 Y. Song, X. Xu, Y. Zhang, Z. Han, J. Liu, J. Li and Y. Zou, *J. Mater. Chem. C*, 2022, **10**, 3387–3395.
4 Y. Zhou, X. Qiu, Z. A. Wan, Z. Long, S. Poddar, Q. Zhang, Y. Ding, C. L. J. Chan, D. Zhang and K. Zhou, *Nano Energy*, 2022, **100**, 107516.
5 J. Y. Kim, J.-W. Lee, H. S. Jung, H. Shin and N.-G. Park, *Chem. Rev.*, 2020, **120**, 7867–7918.
6 W. Yang, J. Hu, J. Chen, Y. Xu, G. Tong, H. Fan, X. Chai, J. Chen and Y. He, *J. Mater. Chem. C*, 2021, **9**, 1303–1309.
7 M. Ahmed, S. Islam and F. Ahmed, *Materialwiss. Werkstofftech.*, 2022, **53**, 790–797.
8 Y. Cao, Y.-L. Tang, Y.-L. Zhu, Y. Wang, N. Liu, M.-J. Zou, Y.-P. Feng, W.-R. Geng, C. Li and D. Li, *ACS Appl. Mater. Interfaces*, 2022, **14**, 48052–48060.
9 X. Chen, T. Zhang, Y. Yu, X. Cai, T. Gao, T. Zhang, H. Sun, C. Gu, Z. Gu and Y. Zhu, *ACS Appl. Mater. Interfaces*, 2021, **13**, 7812–7821.
10 L. Chen, W. Luo, B. Fang, B. Zhu and W. Zhang, *Opt. Laser Technol.*, 2023, **159**, 108924.
11 Y. Wang, C. Xu, L. Yan and J. Li, *Mater. Chem. Phys.*, 2023, **305**, 127935.
12 Y. Ji, W. Xu, I. L. Rasskazov, H. Liu, J. Hu, M. Liu, D. Zhou, X. Bai, H. Ågren and H. Song, *Appl. Phys. Rev.*, 2022, **9**, 041319.

13 L. Shi, Z. Yang, Y. Zhang, Z. Ai, Y. Bao, T. Ma, L. Qin, G. Cao, C. Wang and X. Li, *Sol. RRL*, 2024, **8**, 2300752.
14 Y. Yue, N. Chai, M. Li, Z. Zeng, S. Li, X. Chen, J. Zhou, H. Wang and X. Wang, *Adv. Mater.*, 2024, **36**, 2407347.
15 M. Córdoba, M. Unmüssig, J. Herterich, U. Würfel and K. Taretto, *J. Appl. Phys.*, 2021, **130**, 223101.
16 D. Liu, C. Ding, Y. Guo, H. Li, Y. Li, D. Wang, Y. Yang, Y. Wei, S. Chen and G. Shi, *J. Phys. Chem. Lett.*, 2024, **15**, 5618–5624.
17 C. Zhao, W. Wu, H. Zhan, W. Yuan, H. Li, D. Zhang, D. Wang, Y. Cheng, S. Shao and C. Qin, *Angew. Chem.*, 2022, **134**, e202117374.
18 X. Chen, T. Huang, R. Li, Y. Lin, J. Yang, W. Li and W. Yu, *ACS Appl. Electron. Mater.*, 2023, **5**, 3316–3323.
19 J. Meng, Z. Lan, W. Lin, I. E. Castelli, T. N. Pullerits and K. Zheng, *Nano Lett.*, 2024, **24**, 8386–8393.
20 M. Feng, S. Ye, Y. Guo and T. C. Sum, *Nano Lett.*, 2022, **22**, 7195–7202.
21 B. Yang and K. Han, *Acc. Chem. Res.*, 2019, **52**, 3188–3198.
22 X. Yao, L. Zheng, X. Zhang, W. Xu, W. Hu and X. Gong, *ACS Appl. Mater. Interfaces*, 2019, **11**, 40163–40171.
23 R. Liu, H. Ren, Y. Yu, Z. Zhang, M. Xu, Z. Li and H. Yu, *Sol. Energy*, 2024, **273**, 112527.
24 L. Lei, Q. Dong, K. Gundogdu and F. So, *Adv. Funct. Mater.*, 2021, **31**, 2010144.
25 S. S. Bagade and P. K. Patel, *Phys. Scr.*, 2024, **99**, 052003.
26 Z. Zang, M. Ma, X. Jiang, W. Zhou, C. Seriwattanachai, P. Kanjanaboos and Z. Ning, *Mater. Chem. Front.*, 2024, **8**, 1827–1834.
27 C. Li, R. Zhu, Z. Yang, J. Lai, J. Tan, Y. Luo and S. Ye, *Angew. Chem.*, 2023, **135**, e202214208.
28 H. Zheng, X. Dong, W. Wu, C. Wang, X. Pan and G. Liu, *Appl. Surf. Sci.*, 2023, **610**, 155450.
29 B. M. Lefler, T. J. Houser, A. Chakrabarti, S. J. May and A. T. Fafarman, *J. Phys. Chem. Lett.*, 2023, **14**, 5040–5047.
30 Y. Guo, S. Yuan, D. Zhu, M. Yu, H.-Y. Wang, J. Lin, Y. Wang, Y. Qin, J.-P. Zhang and X.-C. Ai, *Phys. Chem. Chem. Phys.*, 2021, **23**, 6162–6170.
31 X. Zeng, G. Niu, X. Wang, J. Jiang, L. Sui, Y. Zhang, A. Chen, M. Jin, K. Yuan and X. Yang, *Mater. Today Phys.*, 2024, **40**, 101296.
32 L. P. Liao, G. Wang, Y. Q. Yao, L. B. Niu, C. Xu, G. D. Zhou, P. Li and Q. L. Song, *IEEE J. Photovolt.*, 2020, **11**, 99–103.
33 M. Yuan, S. Liu, H. Li, Y. Gao, S. Yu, Y. Yu, L. Meng, W. Liu, J. Zhang and P. Gao, *Adv. Compos. Hybrid Mater.*, 2023, **6**, 55.
34 J. Wan, H. Yuan, Z. Xiao, J. Sun, Y. Peng, D. Zhang, X. Yuan, J. Zhang, Z. Li and G. Dai, *Small*, 2023, **19**, 2207185.
35 C. Li, F. Chen, K. Wang, Q. Yao, J. Zhang, Q. Zhao, Q. Huang, H. Zhu and J. Ding, *J. Mater. Chem. C*, 2022, **10**, 14580–14589.
36 Q. Mo, C. Chen, W. Cai, S. Zhao, D. Yan and Z. Zang, *Laser Photonics Rev.*, 2021, **15**, 2100278.
37 S. Zhao, J. Zhao, S. M. Qaid, D. Liang, K. An, W. Cai, Q. Qian and Z. Zang, *Appl. Phys. Rev.*, 2024, **11**, 011408.
38 S. Zhao, Z. Jia, Y. Huang, Q. Qian, Q. Lin and Z. Zang, *Adv. Funct. Mater.*, 2023, **33**, 2305858.
39 B. Wang, X. Yang, R. Li, S. M. Qaid, W. Cai, H. Xiao and Z. Zang, *ACS Energy Lett.*, 2023, **8**, 4406–4413.
40 Z. Huang, W. Tan, P. Ma, L. Yan, J. Si and X. Hou, *Nanomaterials*, 2023, **13**, 2701.
41 T. Huo, L. Yan, J. Si, P. Ma and X. Hou, *J. Mater. Chem. C*, 2023, **11**, 3736–3742.
42 W. Lin, M. Liang, Y. Niu, Z. Chen, M. Cherasse, J. Meng, X. Zou, Q. Zhao, H. Geng and E. Papalazarou, *J. Mater. Chem. C*, 2022, **10**, 16751–16760.
43 C. Qiu, X. Lin, Y. Wang, G. Feng, C. Ling, J. Liu, J. Du, X. Xiao, X. Wang and P. Zeng, *Adv. Energy Mater.*, 2022, **12**, 2202813.
44 Z. Xiao, T. Tao, J. Shu, W. Dang, S. Pan and W. Zhang, *Crystals*, 2022, **12**, 1425.
45 A. Pandey, A. Vishwakarma, S. K. Saini, M. Kumar and L. Kumar, *Opt. Mater.*, 2023, **146**, 114564.
46 D. Zhao, C. Liang, B. Wang, T. Liu, Q. Wei, K. Wang, H. Gu, S. Wang, S. Mei and G. Xing, *Energy Environ. Mater.*, 2022, **5**, 1317–1322.
47 E. A. Alharbi, A. Krishna, T. P. Baumeler, M. Dankl, G. C. Fish, F. Eickemeyer, O. Ouellette, P. Ahlawat, V. Škorjanc and E. John, *ACS Energy Lett.*, 2021, **6**, 3650–3660.
48 C. Jo, H. Kim, C.-J. Yoon and D.-K. Ko, *J. Korean Phys. Soc.*, 2024, **84**, 17–23.
49 M. Singh, I.-H. Ho, A. Singh, C.-W. Chan, J.-W. Yang, T.-F. Guo, H. Ahn, V. Tung, C. W. Chu and Y.-J. Lu, *ACS Photonics*, 2022, **9**, 3584–3591.
50 M. Duan, Y. Wang, P. Zhang and L. Du, *Materials*, 2023, **16**, 6064.
51 K. M. Dehury, J. N. Acharyya, M. Adnan and G. V. Prakash, *Opt. Mater.*, 2022, **124**, 111969.
52 X. Shen, S. Wang, C. Geng, L. Li, E. Zhao, J. Sun, W. Wu, L. An and K. Pan, *J. Phys. Chem. C*, 2021, **125**, 5278–5287.
53 J. Rieger, J. Hauner, D. Niesner and T. Fauster, *Phys. Rev. B*, 2023, **107**, 125205.
54 T. J. Evans, K. Miyata, P. P. Joshi, S. Maehrlein, F. Liu and X.-Y. Zhu, *J. Phys. Chem. C*, 2018, **122**, 13724–13730.
55 W. Liu, H. Yu, Y. Li, A. Hu, J. Wang, G. Lu, X. Li, H. Yang, L. Dai and S. Wang, *Nano Lett.*, 2021, **21**, 2932–2938.
56 H.-K. Lin, J.-X. Li, H.-C. Wang, Y.-W. Su, K.-H. Wu and K.-H. Wei, *RSC Adv.*, 2018, **8**, 12526–12534.
57 H. Wang, S. Gao, F. Zhang, F. Meng, Z. Guo, R. Cao, Y. Zeng, J. Zhao, S. Chen and H. Hu, *Adv. Sci.*, 2021, **8**, 2100503.
58 H. Guan, G. Mao, T. Zhong, T. Zhao, S. Liang, L. Xing and X. Xue, *J. Alloys Compd.*, 2021, **867**, 159073.
59 I. Ozsahin, B. Uzun and D. Ozsahin, *J. Instrum.*, 2022, **17**, C06003.
60 J. Wang, C. Ling, X. Xue, H. Ji, C. Rong, Q. Xue, P. Zhou, C. Wang, H. Lu and W. Liu, *Small*, 2024, **20**, 2310107.
61 T. Ouyang, X. Zhao, X. Xun, B. Zhao, Z. Zhang, Z. Qin, Z. Kang, Q. Liao and Y. Zhang, *Adv. Funct. Mater.*, 2022, **32**, 2202184.
62 M. K. Kim, J. Cha, H. Jin and M. Kim, *Mater. Lett.*, 2023, **333**, 133577.

63 W. Song, G. Qi and B. Liu, *J. Mater. Chem. A*, 2023, **11**, 12482–12498.
64 H. Yang, A. Konečná, X. Xu, S. W. Cheong, E. Garfunkel, F. J. García de Abajo and P. E. Batson, *Small*, 2022, **18**, 2106897.
65 S. Guan, Y. Ning, H. Chen, B. Huang, B. Zhang and C. Cheng, *J. Mater. Chem. C*, 2024, **12**, 3988–3996.
66 F. Furlan, D. Nodari, E. Palladino, E. Angela, L. Mohan, J. Briscoe, M. J. Fuchter, T. J. Macdonald, G. Grancini and M. A. McLachlan, *Adv. Opt. Mater.*, 2022, **10**, 2201816.
67 M.-N. Zhang, Y. Shao, X.-L. Wang, X. Wu, W.-J. Liu and S.-J. Ding, *Chin. Phys. B*, 2020, **29**, 078503.
68 X. Su, X. Hou, Q. Zhang, Z. Xie, Z. Wei and L. Liu, *Adv. Mater.*, 2023, **35**, 2303964.
69 K. Zhao, J. Zou, F. Huang, T. Tian, Z. Shao, W. Tian, J. Chu and W. Li, *IEEE Trans. Electron Devices*, 2021, **68**, 6266–6272.
70 S. Guan, C. Cheng, Y. Ning, B. Zhang, B. Qin and B. Huang, *ACS Appl. Mater. Interfaces*, 2024, **16**, 41341–41350.
71 X. Sun, Z. Wang, X. Du, D. Zhao, F. Cui, L. Cong and Y. Ren, *Adv. Opt. Mater.*, 2024, **12**, 2302127.
72 J. H. Shen, X. Q. Yu and W. C. Tu, *Adv. Opt. Mater.*, 2023, **11**, 2300410.
73 R. Chen, Z. Liang, W. Feng, X. Hu and A. Hao, *J. Alloys Compd.*, 2021, **864**, 158125.
74 B. A. Huisman, C. Bordoni, A. Ciavatti, M. Sessolo, B. Fraboni and H. J. Bolink, *Adv. Funct. Mater.*, 2024, **34**, 2308844.
75 R. Zhi, J. Hu, S. Yang, C. P. Veeramalai, Z. Zhang, M. I. Saleem, M. Sulaman, Y. Tang and B. Zou, *J. Alloys Compd.*, 2020, **824**, 153970.
76 Y. Liang, F. Liu, X. Xie, Y. Ma, Y. Guan, W. Yu, Y. Zou, L. Zhang, X. Zhang and Y. Zhang, *Adv. Funct. Mater.*, 2024, **34**, 2401257.
77 N. D. Cottam, C. Zhang, L. Turyanska, L. Eaves, Z. Kudrynskyi, E. E. Vdovin and O. Makarovsky, *ACS Appl. Electron. Mater.*, 2019, **2**, 147–154.
78 Y. Liang, Y. Zhang, J. Xu, J. Ma, H. Jiang, X. Li, B. Zhang, X. Chen, Y. Tian and Y. Han, *Nano Res.*, 2023, **16**, 7867–7873.
79 S. K. Shil, F. Wang, K. O. Egbo, Y. Wang, C. K. G. Kwok, S.-W. Tsang, J. C. Ho and K. M. Yu, *J. Mater. Chem. C*, 2023, **11**, 4603–4613.
80 S. Duan, Y. Peng, H. Guan and W. Chen, *Dalton Trans.*, 2024, **53**, 5407–5415.
81 C. Wang, Z. Zhang, X. Zhao, Y. Zhu, M. Li, J. Ding and C. Chen, *Mater. Chem. Front.*, 2023, **7**, 4497–4507.
82 J. Ding, X. Liu, S. Zhou, J. Huang, Y. Li, Y. Gao, C. Dong, G. Yue and F. Tan, *J. Colloid Interface Sci.*, 2024, **654**, 1356–1364.
83 Z. Yang, X. Li, L. Gao, W. Zhang, X. Wang, H. Liu, S. Wang, C. Pan and L. Guo, *Nano Energy*, 2022, **102**, 107743.
84 D. Zhang, C. Chen, J. Huang, H. Wang, Y. Feng and S. He, *Opt. Mater.*, 2023, **138**, 113655.
85 K. Tao, C. Xiong, J. Lin, D. Ma, S. Lin, B. Wang and H. Li, *Adv. Electron. Mater.*, 2023, **9**, 2201222.
86 T. Zhang, Z. Ren, S. Guo, G. Zhang, S. Wang and S. Qiao, *ACS Appl. Mater. Interfaces*, 2023, **15**, 44444–44455.
87 Y. Cheng, Z. Shi, S. Yin, Y. Li, S. Li, W. Liang, D. Wu, Y. Tian and X. Li, *Sol. Energy Mater. Sol. Cells*, 2020, **204**, 110230.
88 J. Yang, C. Li, X. Wei, Y. Huang, D. Wu, J. A. Lai, M. Pi, L. Luo and X. Tang, *Appl. Phys. Lett.*, 2024, **124**, 011106.
89 R. Li, J. Peng, Y. Xu, W. Li, L. Cui, Y. Li and Q. Lin, *Adv. Opt. Mater.*, 2021, **9**, 2001587.
90 J. Wu, Y. Miao, X. Qi, L. Yang, X. Wang, F. Zheng, F. Zhao, S. Shafique and Z. Hu, *ACS Photonics*, 2023, **10**, 4437–4446.
91 B. Moon, J. H. Ahn, M. H. Jeong, S. H. Lee and J. S. Lee, *Adv. Opt. Mater.*, 2023, **11**, 2300414.
92 Z. Xin, Y. Tan, T. Chen, E. Iranmanesh, L. Li, K.-C. Chang, S. Zhang, C. Liu and H. Zhou, *Nanoscale Adv.*, 2021, **3**, 5046–5052.
93 Y. Hou, L. Wang, X. Zou, D. Wan, C. Liu, G. Li, X. Liu, Y. Liu, C. Jiang and J. C. Ho, *Small*, 2020, **16**, 1905609.
94 F. Haque, S. Lim and M. Mativenga, *IEEE Trans. Electron Devices*, 2020, **67**, 3215–3220.
95 F. Haque, M. M. Hasan, E. Bestelink, R. A. Sporea and M. Mativenga, *Adv. Opt. Mater.*, 2023, **11**, 2300367.
96 Y. Che, X. Cao, Y. Zhang and J. Yao, *Opt. Mater.*, 2020, **100**, 109664.
97 H. Xie, P.-A. Chen, X. Qiu, Y. Liu, J. Xia, J. Guo, H. Wei, Z. Gong, J. Ding and Y. Hu, *Appl. Phys. Lett.*, 2023, **122**, 153301.
98 Y. Gao, S. Sun, D. Qiu, Y.-M. Wei, M. Zhang, J. Liu, P. K. Chu, W.-L. You and J. Li, *ACS Photonics*, 2023, **10**, 764–771.
99 S. Tao, D. Yang, G. He, D. Guo, L. Yang, J. Zheng, J. Li, J. Chen and D. Ma, *Org. Electron.*, 2023, **118**, 106800.
100 Y. Fu, Q. Song, T. Lin, Y. Wang, X. Sun, Z. Su, B. Chu, F. Jin, H. Zhao and W. Li, *Org. Electron.*, 2017, **51**, 200–206.
101 M. Jeong, S. G. Han, W. Sung, S. Kim, J. Min, M. K. Kim, W. Choi, H. Lee, D. Lee and M. Kim, *Adv. Funct. Mater.*, 2023, **33**, 2300695.
102 H. Zhang, Z. Zhang, C. Ma, Y. Liu, H. Xie, S. Luo, Y. Yuan, Y. Gao, Y. Zhang and W. Ming, *J. Mater. Chem. C*, 2019, **7**, 5488–5496.
103 M. Jagadeeswararao, K. M. Sim, S. Lee, M. Kang, S. An, G.-H. Nam, H. R. Sim, E. Oleiki, G. Lee and D. S. Chung, *Chem. Mater.*, 2023, **35**, 3095–3104.
104 A. Ishii, A. K. Jena and T. Miyasaka, *J. Phys. Chem. Lett.*, 2019, **10**, 5935–5942.
105 M. Kang, D. H. Lee, J. Kim, G. H. Nam, S. Baek, S. Heo, Y. Y. Noh and D. S. Chung, *Adv. Sci.*, 2024, **11**, 2305349.
106 M. W. Kim, Y. Yuan, S. Jeong, J. Chong, H. Mølnås, A. Alaei, I. J. Cleveland, N. Liu, Y. Ma and S. Strauf, *Adv. Funct. Mater.*, 2022, **32**, 2207326.
107 L. Li, S. Ye, J. Qu, F. Zhou, J. Song and G. Shen, *Small*, 2021, **17**, 2005606.
108 Y. Wu, X. Li, Y. Wei, Y. Gu and H. Zeng, *Nanoscale*, 2018, **10**, 359–365.
109 C. Xie and F. Yan, *Small*, 2017, **13**, 1701822.

110 X. Zhang, X. Liu, B. Sun, H. Ye, C. He, L. Kong, T. Shi, G. Liao and Z. Liu, *ACS Appl. Mater. Interfaces*, 2021, **13**, 44509–44519.
111 J. Sun and L. Ding, *Small*, 2024, **20**, 2308583.
112 C. Li, J. X. Li, C. Y. Li, J. Wang, X. W. Tong, Z. X. Zhang, Z. P. Yin, D. Wu and L. B. Luo, *Adv. Opt. Mater.*, 2021, **9**, 2100371.
113 Z. Zhang, C. Xu, C. Zhu, X. Tong, C. Fu, J. Wang, Y. Cheng and L. Luo, *Sens. Actuators, A*, 2021, **332**, 113176.
114 Y. Zhao, S. Jiao, S. Liu, Y. Jin, S. Yang, X. Wang, T. Liu, H. Jin, D. Wang and S. Gao, *Appl. Surf. Sci.*, 2023, **637**, 157928.
115 K. Xia, W. Wu, M. Zhu, X. Shen, Z. Yin, H. Wang, S. Li, M. Zhang, H. Wang and H. Lu, *Sci. Bull.*, 2020, **65**, 343–349.
116 X. He, S. Hao, D. Ouyang, S. Liu, N. Zhang, Z. Zeng, Y. Zhang, I. Spanopoulos, C. Wolverton and Y. Li, *Adv. Funct. Mater.*, 2024, **34**, 2313163.
117 B. Wang, C. Zhang, B. Zeng, C.-Y. Wu, C. Xie, D. Wu, Y.-X. Zhou and L.-B. Luo, *J. Phys. Chem. Lett.*, 2021, **12**, 2930–2936.
118 J. W. Oh, H. Han, H. H. Kim, H. Lee, D. Kim, J. Lee, J. Kim, W. K. Choi and C. Park, *Adv. Funct. Mater.*, 2022, **32**, 2111894.
119 T. Wang, D. Zheng, K. Vegso, G. Baillard, P. Nadazdy, N. Mrkyvkova, P. Siffalovic, Y. Chen, L. Coolen and T. Pauporté, *Chem. Eng. J.*, 2024, **488**, 151068.
120 S. Liu, S. Jiao, Y. Zhao, H. Lu, S. Yang, D. Wang, S. Gao, J. Wang and L. Zhao, *Adv. Opt. Mater.*, 2023, **11**, 2300831.
121 J. He, C.-Y. Li, D.-X. Qi, Q. Cai, Y. Liu, R.-H. Fan, J. Su, P. Huo, T. Xu and R. Peng, *Nano Lett.*, 2022, **22**, 6655–6663.
122 W. Cheng, S. Wu, J. Lu, G. Li, S. Li, W. Tian and L. Li, *Adv. Mater.*, 2024, **36**, 2307534.
123 Y. Chen, X. Peng, W. Qin, S. Li, L. Zhang, Y. Wang, Z. Chen, B. Yang, Y. Yuan and J. He, *Adv. Funct. Mater.*, 2024, **34**, 2403942.
124 Z. Liu, X. Liu, B. Sun, X. Tan, H. Ye, J. Zhou, Z. Tang, T. Shi and G. Liao, *Adv. Mater. Technol.*, 2020, **5**, 2000260.
125 T. Yan, X. Liu, X. Zhang, E. Hong, L. Wu and X. Fang, *Adv. Funct. Mater.*, 2024, **34**, 2311042.
126 H. Jing, R. Peng, R.-M. Ma, J. He, Y. Zhou, Z. Yang, C.-Y. Li, Y. Liu, X. Guo and Y. Zhu, *Nano Lett.*, 2020, **20**, 7144–7151.
127 R. Xu, L. Min, Z. Qi, X. Zhang, J. Jian, Y. Ji, F. Qian, J. Fan, C. Kan and H. Wang, *ACS Appl. Mater. Interfaces*, 2020, **12**, 16462–16468.
128 A. A. Marunchenko, M. A. Baranov, E. V. Ushakova, D. R. Ryabov, A. P. Pushkarev, D. S. Gets, A. G. Nasibulin and S. V. Makarov, *Adv. Funct. Mater.*, 2022, **32**, 2109834.
129 W. Wang, G. Li, Z. Jiang, Y. Zhang, T. Hu, J. Yi and Z. Chu, *Opt. Mater.*, 2021, **114**, 110926.
130 R. Saraf, H. Fan and V. Maheshwari, *npj Flexible Electron.*, 2020, **4**, 30.
131 M. K. Kim, S. M. Park, H. Jin, J. Cha, D. Baek, T. O. Yoon, G. Lee, S. G. Han, S. B. Jo and S. J. Yang, *J. Mater. Sci. Technol.*, 2025, **207**, 24–33.
132 Y. Zhan, Q. Cheng, J. Peng, Y. Zhao, F. Vogelbacher, X. Lai, F. Wang, Y. Song and M. Li, *Nano Energy*, 2022, **98**, 107254.
133 J. Wang, S. Xiao, W. Qian, K. Zhang, J. Yu, X. Xu, G. Wang, S. Zheng and S. Yang, *Adv. Mater.*, 2021, **33**, 2005557.
134 L. Xue, X. Wang, Y.-Z. Pan, M. Luo, Y. Xu, Y.-W. Li, J.-D. Zhao, Z. Zhao, Q. Li and B.-S. Bae, *ACS Appl. Mater. Interfaces*, 2023, **15**, 54050–54059.
135 L. Mei, K. Zhang, N. Cui, W. Yu, Y. Li, K. Gong, H. Li, N. Fu, J. Yuan and H. Mu, *Small*, 2023, **19**, 2301386.
136 C. Zuo, L. Zhang, X. Pan, H. Tian, K. Yan, Y. Cheng, Z. Jin, C. Yi, X. Zhang and W.-Q. Wu, *Nano Res.*, 2023, **16**, 10256–10262.
137 Y. Zhang, J. Yao, Y. Teng, Z. Zhang, L. Wang, X. Wang, Y. Li, L. Kang, J.-H. He and X. Fang, *Nano Energy*, 2023, **117**, 108915.
138 Y. Wang, S. Bai, H. Liang, C. Li, J. Sun, X. Li, T. Tan, G. Yang and J. Wang, *J. Lumin.*, 2023, **257**, 119700.
139 K. Dong, H. Zhou, W. Shao, Z. Gao, F. Yao, M. Xiao, J. Li, Y. Liu, S. Wang and S. Zhou, *ACS Nano*, 2023, **17**, 1495–1504.
140 Y. Gao, Y. Ge, X. Wang, J. Liu, W. Liu, Y. Cao, K. Gu, Z. Guo, Y. M. Wei and N. Zhou, *Adv. Mater.*, 2021, **33**, 2101717.
141 Y. Cao, Y. Ge, X. Sha, L. Meng, Y. Gao, B. Li, X.-F. Yu and J. Li, *Flexible Printed Electron.*, 2022, **7**, 014013.
142 M. Xia, Y. Li, C. Li, Y. Xu and G. Niu, *Angew. Chem., Int. Ed.*, 2025, **64**, e202425448.
143 L. Liu, S.-Y. Liu, Y. Shi, C.-L. Fang, S. Zhao, H.-Y. Shen, M.-X. Chen, Z.-J. Wang, Y. Ma, Y. Liu, Y. Feng, J. Tang, H.-Y. Ye and G. Niu, *Nat. Photonics*, 2024, **18**, 990–997.
144 J. Wang, S. Yu, H. Jin, Y. Li, K. Zhang, D. L. Phillips and S. Yang, *Adv. Sci.*, 2024, **11**, 2407314.
145 H. Chen, Z. Zhu, B. Zhao, W. Huang, G. Qu, Z.-X. Xu, X.-F. Yu, Q. Xiao, S. Yang and Y. Li, *Adv. Sci.*, 2024, **11**, 2309185.
146 Y. Liang, Z. Zhao, J. Hao, Y. Zhang, D. Chu, B. Jia, J. Pi, L. Zhao, M. Wei, Z. Feng, Y. Li, R. Shi, X. Zhang, Z. Yang, X. Chao, S. F. Liu and Y. Liu, *Nano Lett.*, 2024, **24**, 8436–8444.
147 X. Song, Q. Cui, Y. Liu, Z. Xu, H. Cohen, C. Ma, Y. Fan, Y. Zhang, H. Ye, Z. Peng, R. Li, Y. Chen, J. Wang, H. Sun, Z. Yang, Z. Liu, Z. Yang, W. Huang, G. Hodes, S. Liu and K. Zhao, *Adv. Mater.*, 2020, **32**, 2003353.
148 Z. Han, W. Fu, Y. Zou, Y. Gu, J. Liu, B. Huang, D. Yu, F. Cao, X. Li and X. Xu, *Adv. Mater.*, 2021, **33**, 2003852.
149 Y. Cao, X. Sha, X. Bai, Y. Shao, Y. Gao, Y. M. Wei, L. Meng, N. Zhou, J. Liu and B. Li, *Adv. Electron. Mater.*, 2022, **8**, 2100902.